TECHNISCHE
UNIVERSITÄT
WIEN
Vienna | Austria

DIPLOMARBEIT

Sputtering investigations of wollastonite using solar wind ions

zur Erlangung des akademischen Grades

Diplom-Ingenieur

im Rahmen des Studiums

Technische Physik

eingereicht von

Herbert Alexander Biber
Matrikelnummer 01528891

ausgeführt am Institut für Angewandte Physik
der Fakultät für Physik der Technischen Universität Wien

Betreuung
Betreuer: Univ.Prof. Dr. Friedrich AUMAYR
Mitwirkung: Dipl.-Ing. Paul Stefan SZABO BSc.

Wien, 12.09.2018

(Unterschrift Verfasser) (Unterschrift Betreuer)

Contents

Abstract

As part of Space weathering, ion sputtering by the solar wind alters the surface of airless bodies in outer space. Due to the dynamic process of ejection of particles caused by sputtering and their plunge back to the bodies' surface, a tenuous exosphere is formed. Its composition depends on the surface compounds, which provides the possibility of getting information about the surface via exosphere analysis during flyby missions. Sputtering experiments using wollastonite ($CaSiO_3$) were performed, evaluating mass removal rates for hydrogen and helium, the ions most prominent in the solar wind, for several angles of incident, as this information is needed for precise space weathering models. These measurements were performed using the quartz crystal microbalance (QCM) technique, where the target material is deposited as a thin film on a gold coated quartz. Irradiations were done with solar wind energies of $\sim$1 keV per amu. Results were compared with the outcome of BCA simulations such as SDTrimSP and SRIM. Also of interest was the effect of potential sputtering of He^{2+}, as this is the charge state prominent in solar wind and expected to have a drastic influence on the total mass removal rate. Additionally, charging up effects of the non-conductive $CaSiO_3$ layer were investigated, using several different approaches. Ion current densities were varied over a wide range, an electron flood gun was installed to the target chamber and comparisons using a bulk wollastonite sample were conducted. For the latter experiments, the so-called catcher setup at the Institute of Applied Physics at the TU Wien was used, where a second QCM is placed parallel to the ion beam. Its function is to catch sputtered material and thus measures a resulting mass increase.

Additionally, comparisons of the angular distributions of the sputtered particles for both, the layer deposited on the quartz crystal and the bulk wollastonite sample were performed, also using the catcher technique.

Results for irradiations with solar wind ions show, that kinetic sputtering with helium is well reproduced by SDTrimSP simulations, whereas discrepancies are observed for hydrogen under flat angles. Regarding a charging up of thin target layers, no such effect was observed using the techniques and the setup described, indicating that this does not have any significant influence on the QCM measurements.

Kurzfassung

Sonnenwind-induziertes Zerstäuben, als Teil von Weltraumverwitterung, verändert die Oberfläche von Objekten ohne Atmosphäre im Weltall. Durch den dynamischen Prozess von Teilchenausstoß durch Zerstäubung und deren Fall zurück auf die Oberfläche entsteht eine dünne Exosphäre. Da die Bestandteile dieser von der Oberflächenzusammensetzung abhängen, können Vorbeiflüge Informationen über die Oberfläche liefern. Im Zuge dieser Arbeit wurden Zerstäubungsexperimente an Wollastonit ($CaSiO_3$) mittels einer Quartzkristall-Mikrowaage (QCM) durchgeführt, um die Massenabtragraten für Wasserstoff und Helium, die Hauptbestandteile von Sonnenwind, für verschiedenste Einfallswinkel zu eruieren. Diese werden für präzise Modelle von Weltraumverwitterung benötigt. Bei einer QCM wird das zu untersuchende Material auf einem mit Gold beschichteten Schwingquarz angelagert und aus der Bestrahlungen resultierende Massenänderungen gemessen. Diese Bestrahlungen wurden mit der für den Sonnenwind typischen Energie von $\sim$1 keV pro amu durchgeführt und die Ergebnisse mit den Resultaten aus BCA-Simulationen wie SDTrimSP und SRIM verglichen. Des weiteren war der Effekt der potentiellen Zerstäubung durch He^{2+} von Interesse, da dieser Ladungszustand im Sonnenwind überwiegt und ein drastischer Einfluss auf die Massenabtragrate erwartet wird. Zusätzlich wurden mögliche Aufladungseffekte der isolierenden ($CaSiO_3$) Schicht mittels verschiedener Herangehensweisen untersucht. Ionenstromdichten wurden über einen großen Bereich variiert, eine Elektronenkanone wurde in die Kammer eingebaut und Vergleiche mit einer massiven Wollastonit Probe wurden durchgeführt. Für letztgenannte Experimente wurde der sogenannte Auffängeraufbau am Institut für Angewandte Physik an der TU Wien verwendet, bei welchem eine zweite QCM parallel zur Strahlrichtung eingebaut ist und Massenzunahme durch Einfangen von zerstäubtem Material misst.

Unter Verwendung dieses Auffängers wurden die Winkelverteilungen der ausgestoßenen Teilchen von der auf den Quarz aufgebrachten Schicht und der Wollastonite Probe verglichen.

Die Ergebnisse der Bestrahlungen mit Sonnenwind-Ionen zeigen, dass kinetisches Zerstäuben durch Helium sehr gut von SDTrimSP Simulationen reproduziert wird, wohinge-

gen Diskrepanzen für Wasserstoff bei flachem Einfall zu beobachten sind. Effekte einer möglichen Aufladung der Schicht konnte mit den oben beschriebenen Methoden nicht festgestellt werden, was darauf hinweist, dass dies keinen signifikanten Einfluss auf Messungen mit der QCM hat.

1. Introduction

1.1. Motivation

Objects in outer space are exposed to a permanent stream of different external influences. Especially for airless bodies, this has significant impact on the surface, changing structure and composition. This effect is called space weathering [1] and sums up several effects such as micro meteoroid impact, electromagnetic radiation, solar wind ions and thermal desorption. Its influence on a bodies' surface was observed at the moon, where meteoroid impacts form craters and sputtering processes due to solar wind ions are shown to be responsible for the formation of a darkened crust [2].
Space weathering is not only responsible for surface altering, but those sputtered particles with a kinetic energy too low for leaving the gravitational field of their body of origin return to the surface on a ballistic trajectory. On the moon for example, with a mass of $7.35*10^{25}$ g [3], the escape threshold for oxygen is about 0.5 eV,while sputtered particles energies are typically in the range of up to eV [4]. For most abundances of solar regolith, roughly 60% of the sputtered particles also leave the planets gravitational field [5]. The continuous stream of particles ejected from the surface leads to the formation of a tenuous "exosphere" [6]. The properties of this are depending on the surface composition, so investigations of the exosphere also can give insight to the surface characteristics. Such explorations have already been carried out during flyby missions such as the MESSENGER mission [7]. Flyby analyses have the advantage, that they require no landing on rocky bodies' surfaces. Landing manoeuvre are very difficult to perform and therefore have a high risk of failing, as could be seen during the ROSETTA mission, where the lander PHILAE did not land as planned and was unable to perform the mission as intended [8].
In order to form conclusions on the surface via flyby data, models of exosphere formation and the processes involved are needed. The sputtering contribution is evaluated mainly using SRIM [9] simulations. As these only take the kinetic part of the sputtering into account, experiments using analogue minerals are not only needed to verify simulation outcomes, but also to evaluate the yield due to potential sputtering, which is mainly observed for insulating materials [10]. The outcome can be used to improve

calculations of the total sputtering yield for airless bodies, which can then be used for more accurate exosphere modelling.

Solar wind mainly consists of protons and $^4He^{+2}$ (see figure 1.1), with an energy of about 1 $^{\mathrm{keV}}/_{\mathrm{amu}}$ making up more than 90% of the solar wind flux [11]. Although there are more than ten times more protons in the solar wind than helium, Szabo et al. suggest, that the contribution of He^{+2} to the total sputtering yield is rather significant [12]. This is not only due to the expected high kinetic sputtering yield, but mainly due to potential sputtering. The latter was already observed on anorthite-like ($CaAl_2Si_2O_8$) films [13] as lunar soil simulant.

Wollastonite ($CaSiO_3$) is another candidate for solar wind sputtering investigations. It can be used as an analogue material for pyroxenes, which were found on the lunar surface [14], due to its structural similarity.

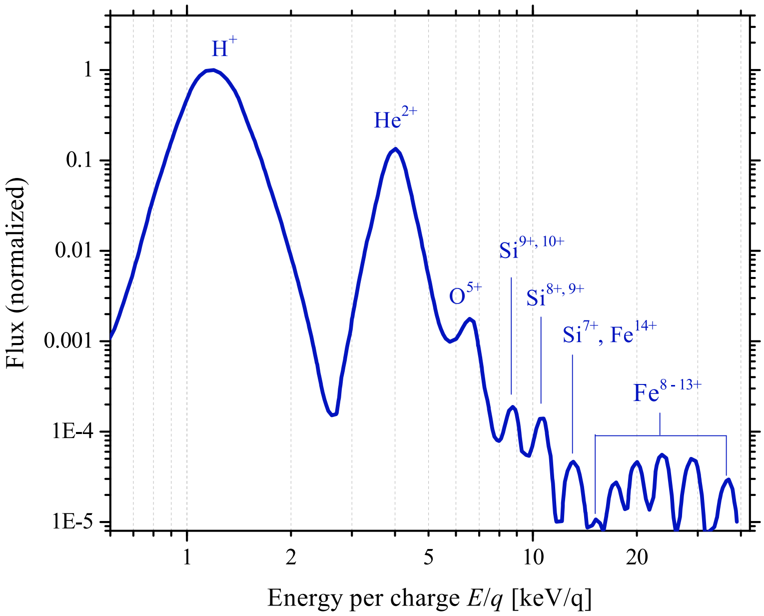

Figure 1.1.: Normalized spectrum of the solar wind ions, where the element abundances are plotted over the energy per charge ratio. The main components are the light elements hydrogen and helium with energies in the range of a few keV. The heavier ions indeed make up only a fraction of the total flux, but due to their higher energies (bigger ratio $^{E}/_{q}$ and high charge states) also contribute to space weathering. Picture taken from [15] with data from [16] and [17].

This thesis aimed on the investigation of angular dependent hydrogen and helium sputtering yields on wollastonite with solar wind relevant energies of 1 $^{\text{keV}}/_{\text{amu}}$. For this purpose, the quartz crystal microbalance (QCM) technique was used, having $CaSiO_3$ coated quartzes irradiated with those ions. Of interest was also the difference between He^+ and He^{+2}, determining the potential sputtering yield of helium on wollastonite. Additionally, a possible charging up of the wollastonite layers on a QCM was tested by varying current densities of hydrogen beams and supplying the target with low energy electrons for its neutralization, using an electron flood gun. Such neutralization tests were also conducted with Argon ions, as a possible charging up effect was observed with these before. Lastly, the so-called catcher setup was used for comparing charging up effects on a bulk sample and the different angular distributions of the particles sputtered from both the QCM and the bulk target.

1.2. Sputtering processes

Sputtering is the process of eroding solids due to ion bombardment with energies in the range of eV up to MeV. Particles are ejected from the surface, when they receive a kinetic energy pointing out of the solid, higher than the surface binding energy. This gives a lower limit for ion energies, as this threshold has to be overcome [4]. The most intuitive type of sputtering taking place is the so-called kinetic sputtering, where projectiles hit a target with certain momentum relative to it, and by this transferring their kinetic energy. This happens with a collision cascade being initialised, distributing the energy onto many atoms [18] and the ion itself continuously looses kinetic energy. The simulation of such a cascade is shown in figure 1.2. With some probability particles in the top layers receive enough momentum perpendicular to the surface for overcoming the binding energy and leaving the solid. This effect is depending on the angle of incidence of the impinging ions, as the location of the cascade varies with it. It is deepest for normal impact and moves up for flatter angles. The angle between the ions initial trajectory and the needed particle velocity outwards of the material gets smaller, typically increasing the number of particles ejected per ion. When going to grazing incident, more ions are getting reflected rather than entering the target material. This effect reduces sputtering again, dropping basically to zero for ions moving perpendicular to the surface. Figure 1.3 shows such a typical dependence of the sputtering yield on the angle of incidence.

On rocky bodies in space, all impact angles are realized, because here surfaces consist of grains and craters of various sizes. Therefore information about the whole angular dependency is needed in order to calculate the number of particles ejected per ion, the so called total sputtering yield.

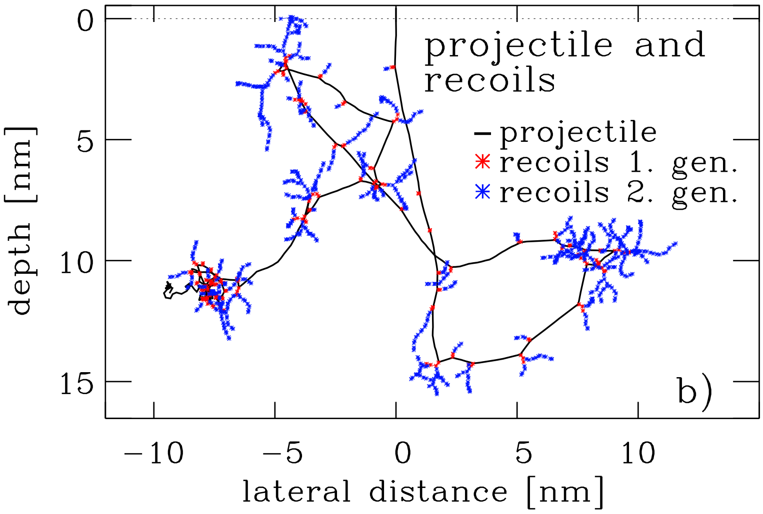

Figure 1.2.: Example for a collision cascade for 2 keV He atoms on a Ni target under normal incident using the BCA software SDTrimSP. The black line shows the helium trajectory, while red points are first generation Ni atoms scattered and blue points indicate second generation. Picture taken from [19]

Not only does sputtering happen due to the transfer of kinetic energy from the ions to the target components, but also from the potential energy carried by the projectiles, as it is the case for higher charged ions. This effect is called potential sputtering, and can only be observed in non-conductive targets, where reduced electron mobility leads to structural changes in the surface [10]. Such targets are found in space, as the lunar surface for example consists partly of insulating pyroxene minerals [14]. Potential sputtering is therefore also an issue for studies of space weathering.

As mentioned, the sputtering yield Y is the number of atoms sputtered away per ion hitting the surface and is the most important quantity for describing sputtering processes. Due to different sputtering yields for each of the components, so-called preferential sputtering, the surface stoichiometry of a compound is changing under ion bombardment until a steady-state is reached. During this process, the mass removal per impinging io is changing as well, which is the quantity observable using the QCM technique. As it is not possible to describe the sputtering yields of the components when using the QCM technique, it is more accurate to use the term mass removal rate, which describes only the average mass removed per impinging ion.

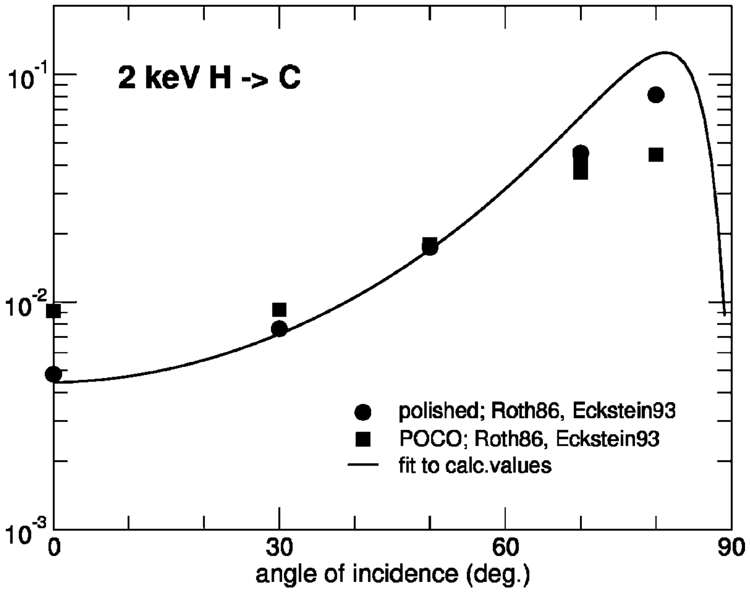

Figure 1.3.: Typical angular dependence of the sputtering yield at the example of 2 keV hydrogen on carbon. Picture taken from [4].

1.3. Quartz Crystal Microbalance Technique

The Quartz Crystal Microbalance (QCM) Technique delivers the possibility for in situ and real time observation of target mass changes as they occur when performing sputtering related measurements. In this method, proposed by Sauerbrey [20], target material is deposited as a thin film of a few hundred nanometre on top of a gold coated quartz. The quartz gets excited to oscillate in its resonant frequency via applying an AC voltage. The mode used is a thickness shear mode, which has an oscillation frequency depending on the thickness of the quartz and is therefore changing during sputtering. An illustration of the QCM Technique and its working principle can be seen in figure 1.4.

The oscillation has anti nodes at the upper and lower borders of the crystal and thus the thickness d_Q is equivalent to the half wavelength λ_0 for the ground mode:

$$\frac{\lambda_0}{2} = d_Q \tag{1.1}$$

When a sufficiently thin layer of material is deposited on the quartz, equation 1.1 is still valid. For a homogeneous target layer, this allows determination of mass changes via repeatedly measuring the resonant frequency of the quartz. This relation is described by the Sauerbrey equation [20]:

$$\frac{\Delta f}{f} = -\frac{\Delta d}{d_Q} = -\frac{\Delta m}{m_Q} \tag{1.2}$$

with the changes in frequency Δf, thickness Δd and mass Δm in the timespan Δt, while f, d_Q and m_Q are the corresponding absolute values of the quartz. With knowledge about material properties of the quartz, one can use the Sauerbrey equation for evaluating the mass change per unit area Δm_A causing the change in frequency Δf:

$$\Delta m_A = \frac{\Delta m}{A_Q} = -\frac{\Delta f \cdot m_Q}{f_Q \cdot A_Q} = -\frac{\Delta f \cdot \rho_Q \cdot d_Q}{f_Q} \tag{1.3}$$

where ρ_Q represents the density and A_Q the Area of the quartz. For sputtering measurements, the current density j, the charge state q of the impinging ions and the elemental charge e_0 can be used for determining the mass removal rate y from equation 1.3:

$$y = -\frac{\Delta m_A}{N_{ion}} = \frac{\Delta f}{\Delta t} \cdot \frac{q \cdot e_0}{j} \cdot \frac{\rho_Q \cdot d_Q}{f_Q} \tag{1.4}$$

When continuously measuring the resonant frequency, one can directly observe the changes in mass in real time and, for constant mass removal, the frequency will increase linear in time. The slope ${}^{\Delta f}/_{\Delta t}$ can then be fitted to determine the mass removal rate.

The quartz used in the experiment was an SC-cut (stress compensated) plano-convex quartz with an eigenfrequency of about 6 MHz. The advantage of an SC-cut quartz is the smaller dependency of the frequency on mechanical stress, which can for example be induced by the clamping of the quartz or by the sputtering process itself.

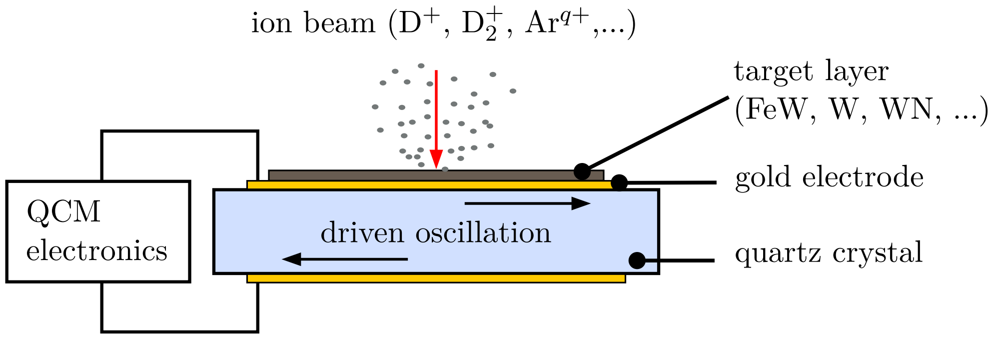

Figure 1.4.: Scheme of a QCM as it is used during the measurements. The AC voltage is applied via the gold contacts and regulated to the resonance frequency of the quartz via specially designed electronics. A thin target layer is deposited on top of the quartz and then bombarded with ions leading to sputtering of the layer. Picture taken from [21].

1.4. Estimations of charging up and the deflection of ions

Due to a possible charging up of the layer deposited on the QCM, this effect is discussed. As a very simplified model, the layer can be seen as a parallel circuit of a capacitor and a resistor. These are fed with a constant current coming from the ions impinging on the surface of the layer. Figure 1.5 shows the scheme of this simple model. For an estimation, one can assume that the current is independent from the voltage across the target layer, giving an upper limit, as the current would only decrease with higher voltage. The following laws were used for this very basic calculation:

Kirchhoff's law:

$$U_R = U_C$$

$$I_R + I_C = I \Rightarrow dI_R = -dI_C$$

Ohm's law:

$$U_R = R \cdot I_R$$

Charge dependent voltage U_C on an capacitor C:

$$I_C(t) = C\frac{dU_C(t)}{dt}$$

From these equations, one can get the well known relation between voltage across a capacitor

$$I_C(t) = C\frac{dU_C(t)}{dt} = C\frac{dU_R(t)}{dt} = CR\frac{dI_R(t)}{dt} = -CR\frac{dI_C(t)}{dt} \tag{1.5}$$

$$\Rightarrow \frac{dI_C(t)}{dt} = -\frac{1}{RC}I_C(t) \tag{1.6}$$

Leading to the well known charging current of a capacitor:

$$I_C(t) = I_C(t=0)e^{-\frac{t}{RC}} \tag{1.7}$$

In this situation however, the current through it at $t = 0$ is whole ion current impinging on the quartz, $I_C(t = 0) = I$. For the time dependent voltage across the target layer follows equation 1.8:

$$U_R(t) = R \cdot I_R(t) = R \cdot I(1 - e^{-\frac{t}{RC}}) \tag{1.8}$$

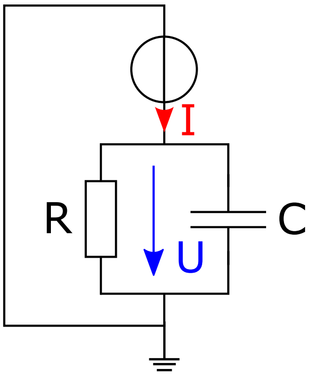

Figure 1.5.: Equivalent circuit diagram of the target layer deposited on the quartz. Resistor and capacitor represent material properties, the current source represents the stream of ions impinging on the target.

For continuous irradiation, the voltage across an insulating target layer is therefore depending on the product of ion current and the resistance of the layer. As only the irradiated area accounts here, this resistance is inverse proportional to this area $R \propto \frac{1}{A_{Beam}}$. By describing the current via its density, one can see, that the beam diameter cancels out and the voltage across the layer only depends on the ion current density j, if outer parameters like the temperature are kept constant.

$$U = R \cdot I = \rho \cdot d \cdot \frac{1}{A_{Beam}} \cdot j \cdot A_{Beam} = \rho \cdot d \cdot j \tag{1.9}$$

Reliable sources for the bulk conductivity of wollastonite could not be found, but some authors suggest a value of of $\sigma = \frac{1}{\rho} = 1.5\ 10^{-11} \frac{1}{\Omega\mathrm{m}}$ [22], which is used for this estimation. Together with an estimated target layer thickness of 50 nm (see section 3.1) and a typical scanned currents of up to 1 nA measured at a 0.6 mm^2 faraday cup therefore give a voltage of about 5 V. As conductivity of the amorphous $CaSiO_3$ layer and its thickness are only roughly estimated here, this value also only gives a guideline. An upper limit for this voltage is however set by the breakdown voltage of the layer, which is for example 620 kV per mm for Al_2O_3 and 560 kV per mm for SiO_2 layers [23]. Again assuming a thickness of 50 nm would lead to a maximum voltage build up of about 25 V - 35 V.
The assumed voltage of the target layer is only one percent of the smallest acceleration voltage used of 1 keV. Changes in velocity in beam direction due to this charging up can therefore be neglected. Considering the movement of the ions in an electrical field perpendicular to its movement and applying simple mechanics, one can find that the lateral deflection is only depending on the ratio between theses two voltages, while being independent on mass or charge of the ions. As shown above, the only relevant parameter therefore is the current density of the beam.
Summing up the estimations made, one would not expect significant effects on the experiments due to charging up of a thin $CaSiO_3$ layer.

2. Experimental setup

2.1. Beamline

The ion beam used for bombarding the QCM in the performed measurements was produced in the 14.5 GHz electron cyclotron resonance (ECR) ion source SOPHIE at the Institute of Applied Physics at the TU Wien. In an ECR ion source, working gas is heated by microwave radiation and confined in a magnetic field. The gas is therefore injected in a discharge chamber where electrons are excited to perform cyclotron motion in the magnetic field using microwave radiation. Collisions between these and the working gas lead to heating and ionisation. Therefore a plasma is formed, which is confined in a so-called "minimum B" magnetic field configuration, consisting of an axial magnetic mirror field and a radial hexapole field. Ions leaving the source, do so as a beam via a so-called "accel-decel" extraction system. It consists of three insulated electrodes and is used for suppressing the electrons and optimising the ion beam. The SOPHIE can be put on an electrical potential of up to 6 kV, which is sufficient for solar wind energies of 1 keV/amu when using hydrogen and helium, the elements most prominent in the solar wind. Detailed informations about the ion source can be found in [24] and [25].

Directly after leaving the source, the beam is passing through two quadrupole electromagnets. These are used for focusing the beam, which is done via maximising the current measured in the faraday cup in the experimental chamber (see section 2.2). A dipole magnet is then used for m/q selection of the desired ions, deflecting them into the beamline. Via continuously varying the current through the magnet coils, a mass over charge spectrum of the beam can be taken. This is usually done after SOPHIE was turned on, as the needed magnet current varies due to hysteresis and peaks can be close to each other. Taking a full spectrum makes it possible to identify the needed settings much better. For measurements using $^{4}He^{2+}$, the magnet is not sufficient to guarantee a pure ion beam. With a mass over charge ratio of 2 $^{4}He^{2+}$ ions cannot be distinguished from hydrogen molecules H_2^+. As hydrogen is present from water in the atmosphere, the ion source is contaminated with it. This is aggravated by the fact, that hydrogen is hard to pump with turbo molecular pumps, due to its small mass. The contamination is taken into account, when evaluating the measurement data in section 3.3.

Last part in the path of the beam before entering the experimental chamber is a faraday cup mounted on a manipulator, which can be placed after the sector magnet. As it is closer to the magnet than the experimental chamber, it is used for pre-adjusting the ion beam and for taking the mass over charge spectra, because signals are bigger here. It is in one line with the target holder zero position and therefore allows a good guiding of the beam towards the centre of the experimental chamber. A schematic of the beam path from source to target holder is shown in figure 2.1.

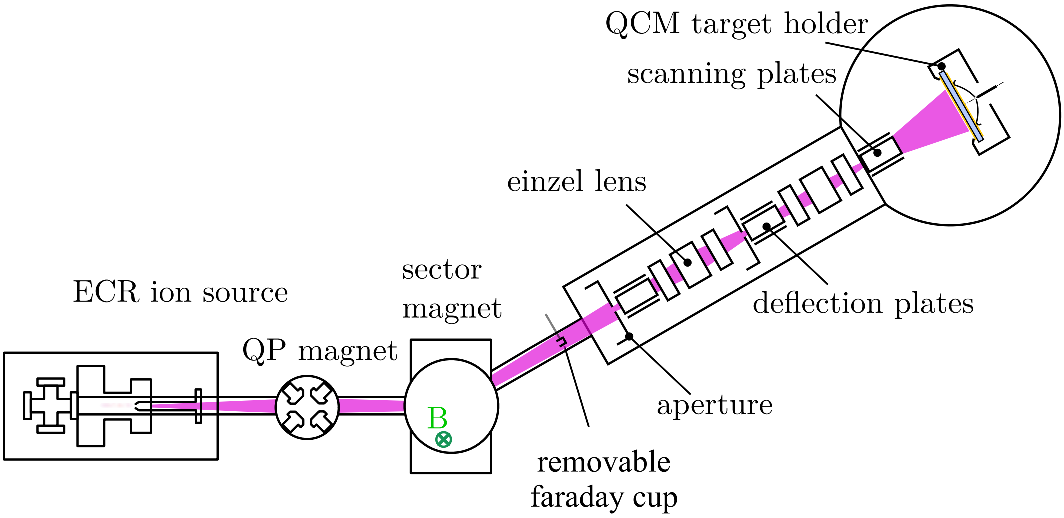

Figure 2.1.: Scheme of the ion beam path used for the conducted measurements. Working gas is ionized in the ECR ion source and accelerated due to the a potential difference to the grounded rest of the system. It is then focused and deflected in the magnets, where also m/q selection is made. Fine adjustments and scanning of the beam are then happening in the experimental chamber, using electrical fields. Picture adapted from [21]

2.2. Sample chamber

When entering the target chamber, a system of electrostatic lenses and deflection plates is guiding the ions towards the target holder zero position. After the beam is focused and aligned correctly, it is scanned over a desired area using a pair of scanning plates. These are operating with two sawtooth voltages at 1.6 kHz and 50 Hz, leading to a homogeneous irradiation of the sample. Their signal amplitudes can be varied separately, which can be used for experiments with different current densities as they were performed. The holder itself can be moved along all three axes and rotated perpendicular to the incoming beam, allowing the measurement of angular dependent sputtering yields. Furthermore, due to the possibility of movement in beam direction, the position between the catcher QCM (see below) and the target can be varied. Such measurements can give information about the distribution of sputtered particles. The holder carries a faraday cup for measuring the ion beam current, a QCM with target material deposited on it and a clamping device for bulk materials (see figure 2.7). This is used for comparing sputtering yields of bulk targets and deposited films using a catcher method as discussed in the next section. Due to their mounting directly above each other, these measurements can be performed without the need of changes in the chamber directly during the same irradiation sequence. Experiments are performed under UHV conditions, with pressures in the range of typically 10^{-10} mbar, where the mean free path for the projectile ions is in the order of kilometres and collisions with residual gas can be neglected. Furthermore, such pressures are needed to ensure that the surface is not altered by the remaining gas molecules during the experiments, as the formation of a layer of residual gas molecules affects the sputtering yield.

2.2.1. Catcher setup

As mentioned in section 1.3, the QCM technique allows very precise determination of sputtering yields via measuring the resonance frequency of a quartz crystal. Therefore, target material has to be deposited onto such a quartz as a fairly thin layer of maximal some hundred nanometres. This is not a problem for smooth, elemental targets, as the composition cannot change and surfaces can be produced very flat [26]. When dealing with more complex targets however, this method is limited. Composed materials, such as the $CaSiO_3$ used for sputter experiments during this thesis for example need to be deposited using methods like pulsed laser deposition, reproducing the original stoichiometry as precisely as possible [27]. Nevertheless, the relative abundances differ from the original sample to some degree and can vary between several batches, as is mentioned in section 3.1. Another example of limitations are specific surface structures, like a RMS roughness of some hundred nanometres. Realistic targets however often have such properties, making it challenging to investigate their sputtering behaviour using the classical QCM technique.

The so-called catcher-setup was developed in order to overcome these limitations and to measure sputtering yields of bulk targets instead of thin deposited layers. Here, a microbalance is used as catcher (C-QCM), capturing material ejected from the original sample. The resonance frequency then decreases due to the new material being deposited on it. This is possible, because energies of particles leaving the surface due to sputtering is typically less than 50 eV and sticking can occur, as it is used during sputter deposition processes [28], [29]. However, the sticking parameter describing this probability is depending on both target material and species of the atom being ejected, which makes it difficult to correctly interpret measurement results.

The C-QCM used for the measurements is placed on a linear manipulator, which is perpendicular to the ion beam and the rotatable axis of the target holder, schematically shown in figure 2.2. It can be moved as close to the target as desired, which is necessary for getting sufficient signals, since the particle flux density follows a $1/r^2$ law and only a fraction of the solid angle with respect to the target is covered.

When using this technique, several factors have to be taken into account, which are not present or can be neglected when irradiating a QCM directly with an ion beam, as there were [30]:

1. The target material is emitted from an extended area and with a certain angular distribution
2. Emitted particles hitting the C-QCM can either stick on it or get reflected
3. Ions getting reflected from the sample can lead to sputtering of the catcher, reducing the signal
4. The sensitivity of quartzes is not uniform but follows a gaussian distribution

With the sawtooth voltages at the scanning plates, the ion beam is homogeneous over a desired area, but has a not very well defined decrease to zero at the border. This is not a problem for measurements at the target quartz, because there it is only important to have a constant current density over the sensitive area of the quartz for the Sauerbrey equation to be valid (see 1.3). Particles hitting outside of it do not alter the signal and can therefore be neglected. For the catcher setup however, the beam must not vary over the irradiated area, since the intensity for every point must be known for precise analysis. Furthermore, the ion beam must be focused on the target without hitting the holder around it, since this would lead to sputtering there and deposition on the C-QCM as well, giving a false signal. To fulfil both requirements, a system of apertures is placed on a linear manipulator between scanning plates and target, allowing to choose diameters of 2, 3, 4 and 7 mm. Of course it can be completely removed from the ion beam as well, which is necessary for adjusting the beam after the ion source was turned on. The variety of sizes is needed, because the projected target area is reduced when the target is turned, while diameters bigger than 3 mm are favourable when irradiating the quartz, since its sensitivity is depending on the size of the irradiated area (see below). In addition, this aperture allows a qualitative observation of the beam stability during a measurement. For this purpose, instead of simply putting it on ground potential, it is connected to a picoamperemeter, logging the measured current on a PC. This can be very useful if the slope of the frequency change is not constant due to fluctuations in the ion current. If such are present, they are observed at the aperture current and can be directly linked to the unstable slope. On the other hand, it allows to rule out ion current instabilities, if the current measured at the aperture is constant. Figure 2.3 shows an example of such a pair of current at the aperture and slope of the quartz frequency. The slope there was calculated using a Savitzky–Golay filter with a length of 50 data points and 5 iterations. At the end of the irradiation, a spike can be seen, which might be related to outgassing of helium in the quartz. A spike going downwards at the beginning did also occur, but is not seen in this figure. Such an effect can often be observed during QCM measurements and is probably linked to implantation and gassing out of projectiles or energy transfer to the quartz. However, one can clearly see, that the fluctuations in the QCM signal are very well reproduced by the current measured at the aperture, even without shifting or rescaling one of the signals. As there is no one to one correspondence, this can only be used to make qualitative statements about the beams stability.

The aperture system was also used for irradiating the QCM target, and as the Sauerbrey equation is only valid for homogeneous mass removal on the whole quartz, this reduction of the ion beam diameter to smaller sizes than the actual quartz leads to deviations from the results for irradiation over the full area. This influence can be determined using

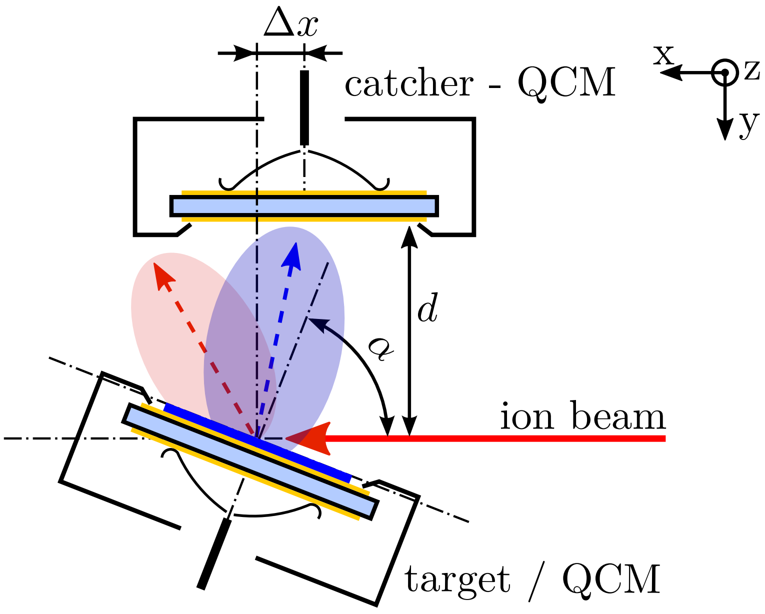

Figure 2.2.: The catcher setup is shown schematically, with the C-QCM perpendicular to the impinging ion beam. The distance d can be varied via the catcher manipulator, Δx and α via shifting or turning the target quartz. Bulk samples can be used as target for the ions instead of a QCM as well. Figure taken from [21].

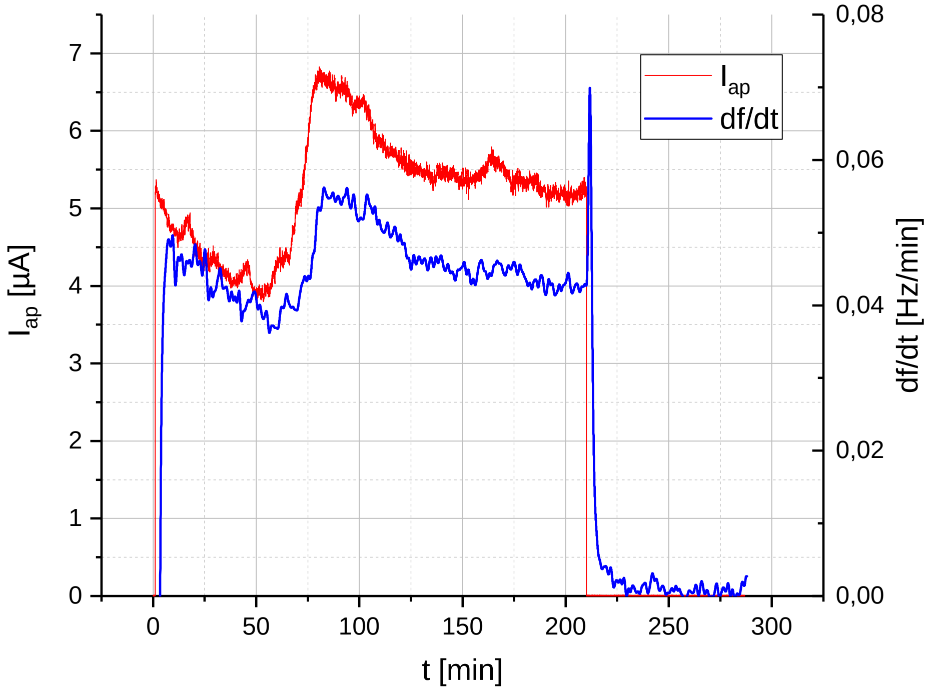

Figure 2.3.: Current measured at the aperture in front of the QCM target together with the local slopes of the quartz signal. This was generated using a Savitzky–Golay filter with a length of 50 data points and 5 iterations. The spike in the end is related to a steep increase in frequency when the beam was turned off, which is a feature often observed using the QCM technique but not influencing the measurements. Very good qualitative agreement between both curves allows linking the quartz instability to the ion current.

the amplitude function $a(x,y)$ for the quartz, as only its innermost part is sensitive to mass changes anyway [21]:

$$a(x,y) = e^{-\frac{1}{2}(\alpha x^2 + \beta y^2)} \tag{2.1}$$

with ${}^{\alpha}\!/_{\beta} \approx 0.8$ being parameters depending on material properties of the quartz. It is sufficient to use an average value, and therefore assume a radially symmetric amplitude function. The sensitivity $s(r)$ of the quartz is proportional to the square of the amplitude function $a(r)$ and describes its sensitivity to mass changes. In order to calculate the difference between the signal with a reduced beam diameter, the sensitivity has to be integrated over the desired surface. An estimation of the upper limit of the difference for the 4 mm aperture used during QCM irradiations, this can be done for 0°, resulting in the smallest irradiated quartz area. Including the divergence of the beam between aperture and target caused by scanning, the beam diameter at the quartz is about 5 mm. In this case, the deviation from the signal obtained when irradiating the whole quartz is only 1.5% and is even smaller for bigger angles, because the projected area increases there. As the uncertainty of the current is assumed to be 10%, it is reasonable to neglect the effect of reduced beam diameter for the evaluation.

The catcher quartz only covers a fraction of the solid angle for the target quartz, which in addition to the factors mentioned above, leads to a signal much smaller than the one on the target QCM. Drifts of the frequency, which for example appear with small changes in the lab temperature, therefore play a much bigger role, as their size compared to the signal becomes bigger as well. In section 3.5, an example for such a signal can be seen, where air condition driven oscillations in room temperature with a period of about one hour also result in frequency oscillations in the range of the signal obtained during irradiation. One attempt to tackle this problem is to irradiate for longer periods of time, where these oscillations can be averaged out. This has the major drawback, that measurement times are very long, not only limiting the amount of data obtainable, but also bringing the risk of long time fluctuations of the ion beam for example. Another solution for this problem was found by packing the fast electronic circuit attached to the vacuum chamber between two 10mm thick aluminium plates, since oscillations were found to be mainly caused due to changes of this circuits temperature, but not of the quartz. These plates act as a heat reservoir, damping the changes in circuit temperature.

The positive effect of these plates can also be seen in section 3.5, where signals with and without them are shown.

2.2.2. Target chamber setup including electron flood gun

The contribution of potential sputtering to the total yield is so far known as to be independent from the angle of incidence. However, some previous unpublished measurements using argon as projectiles showed a decreasing yield for higher charge states when irradiating under flat angles. A possible explanation for this behaviour could be a charging up of the insulating wollastonite layer. In order to verify, whether this effect takes place, an electron flood gun was installed in the target chamber, which is typically used to supply insulating samples with low energy electrons when performing XPS or SIMS analysis. The purpose of these electrons is to neutralize a possible build up of positive charge on the insulating $CaSiO_3$ layer. Figure 2.4 shows the flood gun placement in the target chamber. Due to the chambers setup, mounting it in the line of sight of the quartz was not possible without massive reconstruction. Instead, it had to be mounted in a cylinder attached at the side, pointing towards the cylinder's other wall. The gun can deliver several µA of electrons with energies of 0 to 80 eV. Due to the fairly high backscattering rate [31], one can assume, that some electrons are absorbed directly at the walls of the vacuum chamber, but a fraction is also scattered several times. They are therefore available for neutralisation in the whole chamber and should be able to prevent a possible charging up of the wollastonite layer.

The flood gun itself consists of a filament, which can be varied in its potential, also changing the electron energies. After this filament, a grid is placed, allowing a reduction in electron current without changing their energies. It can be set to potentials from zero upwards and was used for the measurements discussed in section 3.4. The flood gun also features a focusing system and deflection plates, allowing to guide the electrons towards a target. Due to the positioning in the chamber, these adjustments had only an marginal effect on the electron current measured at the target position. A scheme of the flood guns build-up can be seen in figure 2.5. The controls feature two modes of operation, one delivering electrons with a fixed energy of 500 eV and another one allowing to set a desired value from 0 to 80 eV, using a potentiometer. The control module also allows monitoring of parameters such as extraction- and grid potential or emission current via

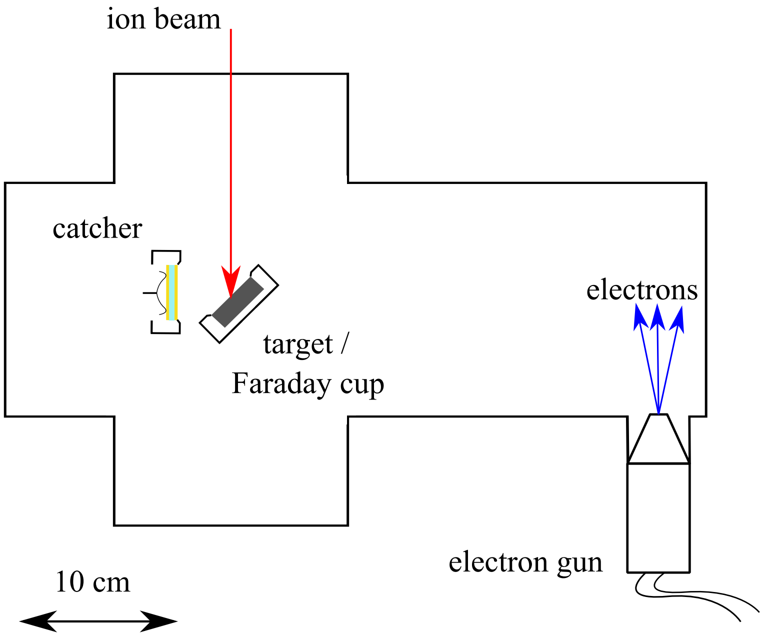

Figure 2.4.: Position of the electron flood gun in the experimental chamber. Although it is not pointing to the target, a sufficient amount of electrons arrived at that position, as they are scattered from the surfaces several times [31].

a display.

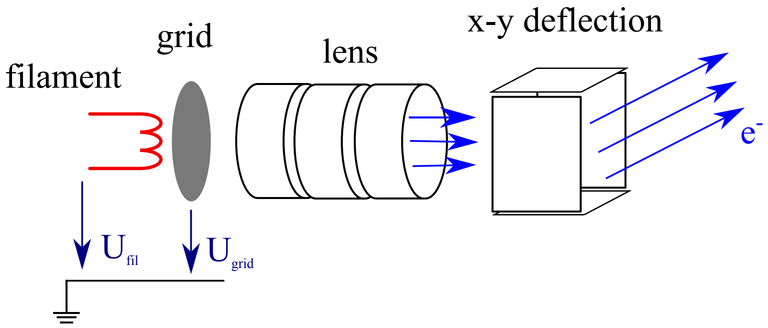

Figure 2.5.: Scheme of the electron flood guns internal build up. Electrons are emitted from a filament and can be partially blocked using a grid, with both parts being at adjustable potentials. Focusing and guiding is achieved using electrical fields.

In order to verify the availability of a sufficient amount of electrons at the target, first tests were performed, measuring the electron current at the faraday cup. A detailed description of these measurements and its results can be found in section 3.4.2. As mentioned there, most of the electrons are detected at the back side of the faraday cup, as most of the exposed area is due to the connector and the current measured is only slightly depending on the cups suppressing voltage. However, the maximum electron current measured at the faraday cup was set by varying the heating wire potential, while choosing operation mode and varying electron energy and grid potential. Several reasons argue against the mode operating at 500 V, such as a smaller current at the faraday cup, a less prominent attraction and possible stimulated desorption. Thus, only the variable mode with up to 80 eV was used during experiments. The maximum current was found to be at an extraction voltage of about 30 eV, which was the energy then used during most of the measurements with active flood gun. For the variation of the grid potential, it was found, that the current at the target position is maximal with the grid at ground potential and is monotonically decreasing for increasing voltage and can be seen in figure 3.7a in section 3.4.2. This was used for determining the effect of delivering electrons, as the current was reduced stepwise to zero.

After installation or opening of the vacuum camber, a degassing procedure has to be performed, which is described in the electron gun's manual in detail. During this period, the pressure must not exceed $5 \cdot 10^{-8}$ mbar, and deposition of material on the quartz can be observed during this time. It then takes several hours of operation, until the quartz signal shows no more response to the electron gun being turned on. This is probably related to material getting desorbed from the guns inner wall. Nevertheless, even afterwards, turning on electron emission always increased the pressure by one order of magnitude, from about 10^{-10} mbar to 10^{-9} mbar. This increase was almost instantaneous, but the decrease after turning off was not. Therefore this can be attributed to a real pressure increase and not just an effect the additional electrons in the chamber have on the pressure gauge.

Modified setup including bulk sample

As mentioned above, materials have to be deposited as a thin film onto a quartz crystal, in order to be investigated using the QCM technique. This limitation can be overcome using the catcher setup, as a mass increase on a secondary microbalance due to sticking of sputtered material is detected here. The sputtering yield of wollastonite was mainly investigated using the classical QCM technique, having $CaSiO_3$ deposited on a quartz crystal. In addition, measurements using the catcher setup were performed, irradiating both the QCM target and a bulk sample of wollastonite as well. Therefore, the target holder had to be redesigned, adapting it for this purpose, as a mounting mechanism for the bulk wollastonite was missing. It is based on the previous version, including faraday cup and the microbalance in the same positions as before. This allows usage of the classical setup without any adaptation to the new target holder. The clamping mechanism for the bulk sample is added at the bottom end of the previous version. An important aspect of the design was, that changes between QCM and bulk target should be uncomplicated and fast to perform. Therefore, the surfaces of the new target has to be in the same plane as the quartz crystal ones. Otherwise, shifts in both x- and y-direction would be necessary when changing between the targets (see figure 2.2). By additionally setting the same phase on the hole as for the quartz holder, limitations of the angle of incidence of 70° apply to both targets.

A technical requirement was the feeding of the QCM heating wires to the backside of the holder. This is needed, as the feedthrough connectors come from a flange there, and routing the cables on the side could lead to either them getting stuck or touching of the

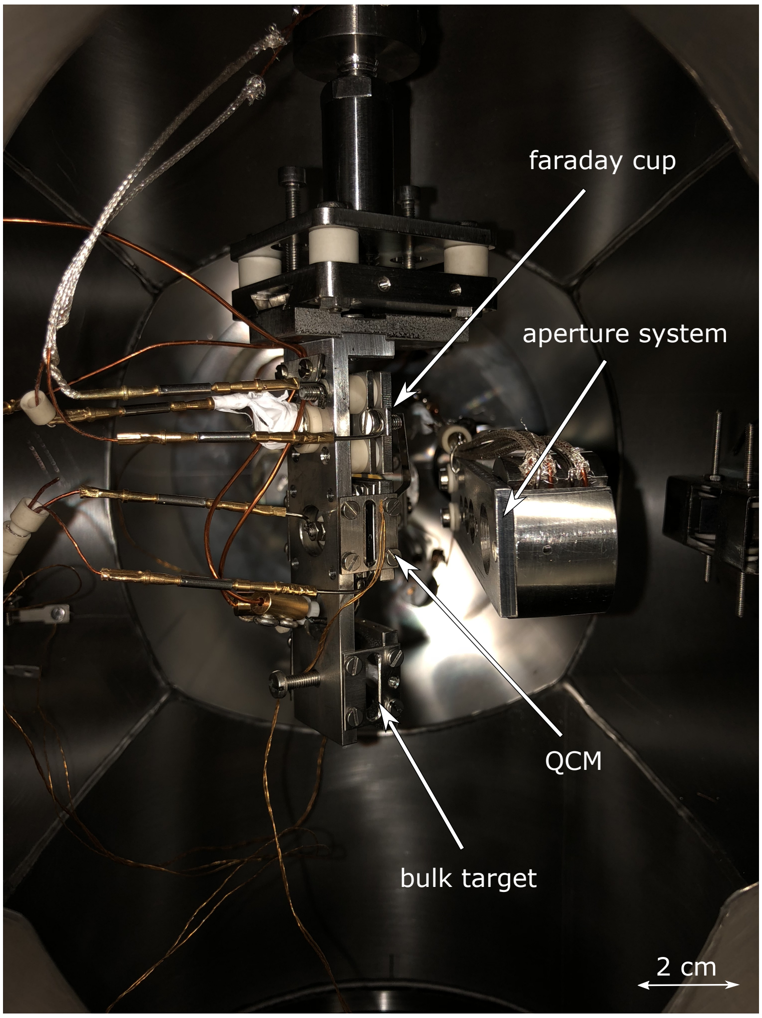

Figure 2.6.: Picture of the target holder, carrying the faraday cup in the upper third. The cup itself is wrapped with Teflon tape on its backside and the suppressing voltage applied at the side. For ions, the detection happens directly in the cup for those entering it through the aperture, but electrons moving around in the chamber are measured at all non insulated or shielded parts connected to the cup, such as the connectors or the cups outer side. One can also see the QCM in the middle and the bulk wollastonite sample in the lower part of the target holder.

conductive clamps. Furthermore, this allowed fast swapping of the old target holder, without having to remake the heating wire.

Considering the positioning of the sample, threads are placed on the side and the bottom of the front plate. These can be used for clamping of the sample using setscrews, holding it in position. The screw coming from the target holder base can be used to push it against the front plate, applying pressure and ensuring alignment there. For samples big enough to cover the whole front plate opening, the setscrews can be left in, after the base screw is in place, otherwise they should be removed. For smaller targets ions can hit the setscrews, leading to sputtering and a false signal at the C-QCM. Figure 2.7 shows a visualisation of the new target holder CAD assembly, with the part for clamping of bulk samples in the lowest section. For illustration purposes, a sample is shown there, held in place via the screw on the back. As it is smaller as the opening in the front plate, the setscrews on the sides would have to be removed in such a case after the mineral is in position. Drawings of the new and redesigned parts can be found in the appendix.

The piece of wollastonite placed in the experimental chamber comes from the same base material, as the one used for depositing a thin film on the QCM. It was sanded using a *Struders LaboPol-4* wet sanding machine with wet grinding paper and active water flow. In a first step, 1000 grain paper was used to create a continuous, flat surface. Afterwards, this plain was sanded finer using a 2400 grain paper for 5 minutes at maximum speed. As the atomic force microscope analysis shown in section 3.1 reveal, this lead to a surface with a RMS roughness of only 3.2 nm. Because this material is quite brittle, it broke apart several times during its preparation. This is why the sample built into the chamber does not fill the whole available area of the target holder, which is however not a problem for measurements, due to the aperture system. As the projected length perpendicular to the rotation axis getting reduced when turning the sample, the long side was to be orientated in this direction.

2.2.3. QCM electronics

As mentioned in chapter 1, sputtering yields are determined via driving quartz crystals at their resonance frequency. Electronics specially developed for this purpose were used, basically consisting of two parts, a fast circuit directly attached to the vacuum chamber and a voltage controlled oscillator[32]. They are connected via signal, power

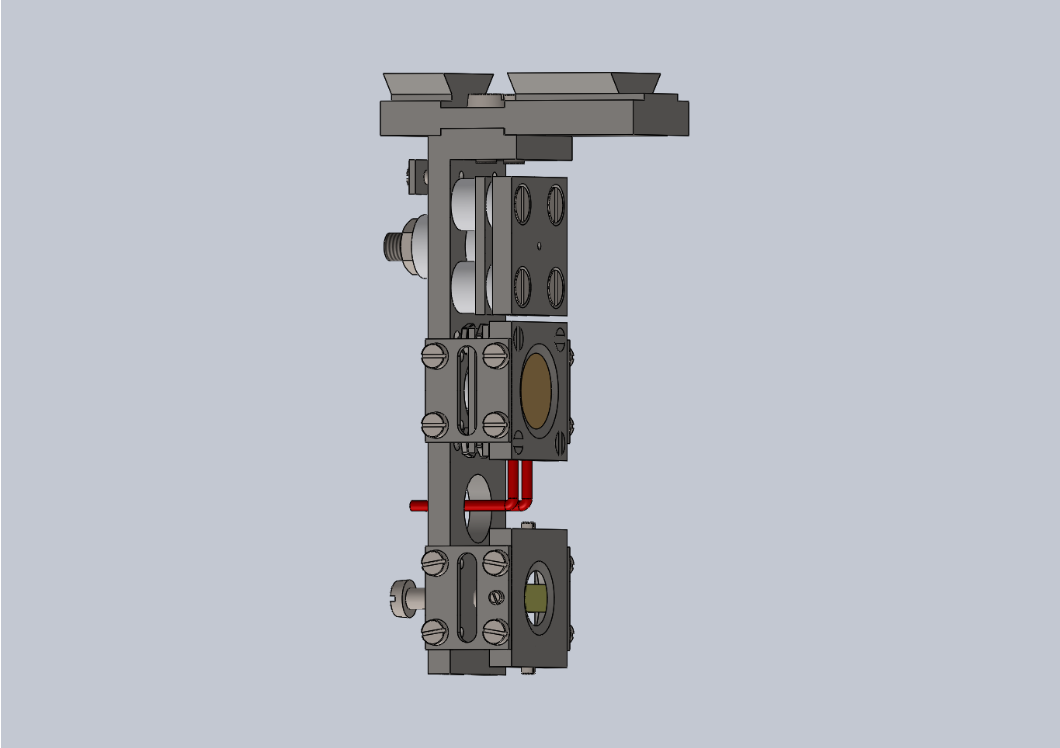

Figure 2.7.: 3D visualisation of the new target holder design, with the clamping for bulk samples in the lower part. Such a sample is illustrated, only being hold in place via pressing from the screw in the back. The setscrews should be removed after installation of the stone, as they are not covered by the sample, which could lead to their irradiation.

and feedback line, so that the fast circuit is placed between quartz and oscillator. It is often referred to as phasebox, because it gives feedback to the oscillator, depending on the phase shift of the current through the quartz. This is a DC voltage, changing its sign at resonance frequency of the quartz, which the oscillator can regulate on.
All cables, including power supply and DC feedback voltage as well as both circuits are shielded, in order to keep interference with other signals out of the system.

Basics of the voltage controlled oscillator

The frequency of the oscillator is controlled via a low noise LC oscillator, which is tunable between 59 and 96 MHz by a varicap, noted by their type (BBY40) in the schematics in figure 2.8. The coil L1 is the inductance of this resonator circuit. Via applying voltage at the VC_{in} connection, the integrator increases potential at the varicaps cathode continuously, ramping up the oscillators frequency. A negative input voltage however decreases it, having a stable working point at 0 V input. The RF signal is internally rectified and converted to TTL levels and directed to an output, which is measured using a frequency counter controlled via a logging pc. It is also going into a Johnson counter, dividing it by a factor of 10, sinusoidally shaped using a filter. After buffering using IC13 the signal is directed to the phasebox and therefore the quartz crystal.

Working principle of the phasebox

As can be seen in the schematics (figure 2.9), the circuit consists of two branches, with its symmetry being broken by the quartz on one side (Pin 12 of IC2). Due to the current sources, the RF current has to pass the 47pF capacitors, leading to a phase shift between the two branches, if the quartz is in resonance. The two collectors are connected to a multiplier, giving a feedback depending on the phase between these signals. When the quartz is in resonance, this shift is 90°, leading to zero volt feedback. As mentioned above, the sign of this DC-feedback voltage changes when passing this point, while the voltage controlled oscillator can regulate at this change of sign and the quartz's oscillation is therefore kept at resonance frequency.
The cable indicated in the second branch at the schematics is a dummy line, which is also fed into the vacuum chamber, leading directly to the quartz. As theses cables are in both branches, this allows compensation of the cable capacity.

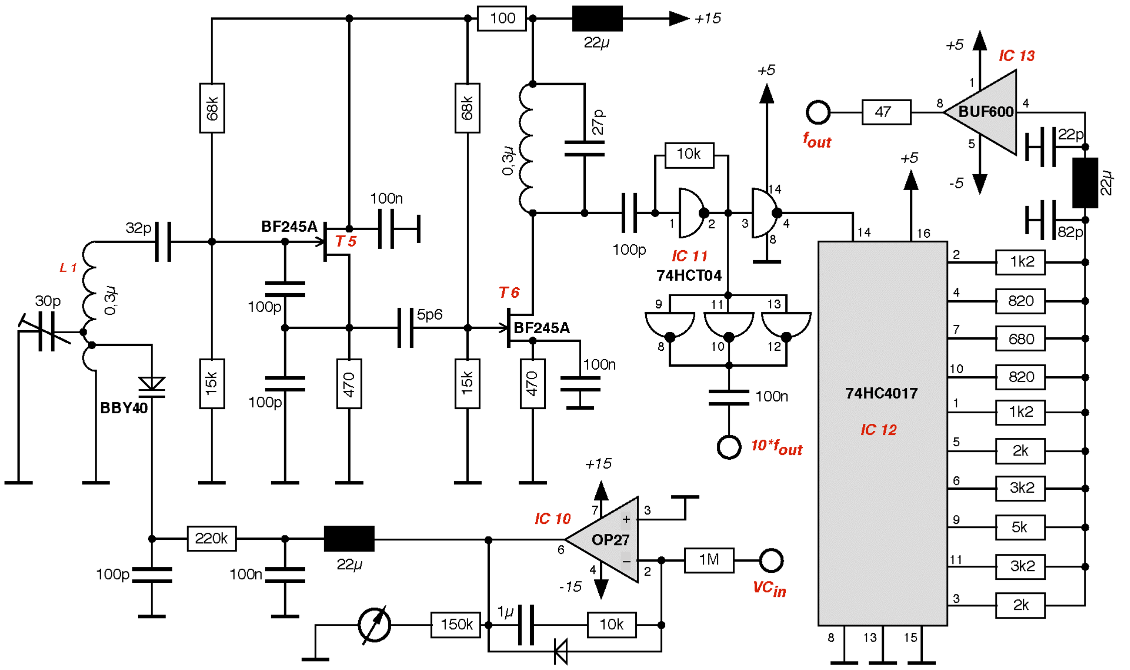

Figure 2.8.: Schematics of the voltage controlled oscillator, consisting basically of an integrator, a variable LC resonator and a Johnson counter. Image taken from [33].

A more detailed description of the working principles of both phasebox and voltage controlled oscillator can be found in [33].

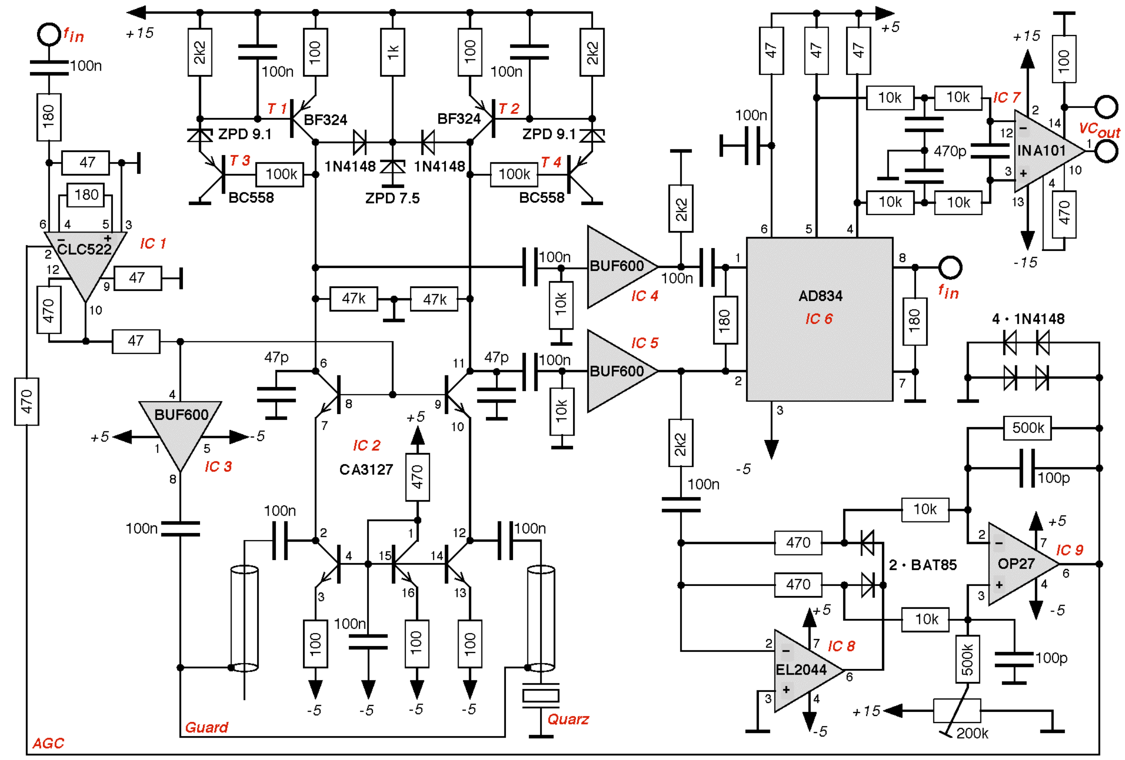

Figure 2.9.: Circuit of the so-called phasebox, taken from [33], where a detailed description can be found. The CA3127 transistor array (IC2) and the three buffer amplifiers BUF600 (IC3-5) were broken and replaced.

Repair of Phasebox

One of the used phaseboxes was broken and had to be repaired. Since the design itself was established twenty years ago, many of the integrated circuits used are not longer available. Possible replacement parts were searched for and are listed in table 2.1. For the HFA3127 transistor array (IC2), the minimal breakdown voltage V_{CE} is only 12 V instead of 20 V as it is for the original CA3127. Therefore the protective zener-diode with a breakdown voltage of 7.5 V has to be replaced in order to maintain some protective effect. A suggested value here is 3.2 V, allowing a potential of about 4 V on Pin 11

of IC2. The other replacements should work without adaptations in the schematics, but as mentioned below, only the HFA3127 and the LMH6559 were tested during repair.
In order to find the broken parts in the phasebox, the two branches of the circuit were checked for symmetry, without a quartz being attached. A 6MHz sinus signal from a function generator was fed into the circuit. Checking the voltage at Pin 6 of IC2 showed a DC-signal, while Pin 11 had a distorted sinus on it. Further investigation of the transistor array using a multimeter showed broken transistors there. Together with the protective zener-diode, it was replaced with a HFA3127. Further analysis after this replacement showed, that the BUF600 buffer amplifiers IC4 and IC5 were also broken. Their maximum input current is rated 3 µA, leading to a voltage of 3 V at the input, considering the 10 k resistor to ground. This voltage was above 3 V, indicating an input impedance smaller than allowed. Furthermore, the well shaped sine input was distorted at the output, also indicating that these parts were broken. After these were replaced with LMH6559 SMD-ICs and adapter boards (SOIC8 to DIP8), the phasebox worked properly.

original	BUF600	CLC522	CA3127	EL2044	OP27	AD834	INA101
new part	LMH6559	LMH6503	HFA3127	ISL55001	OP27	AD834	INA101

Table 2.1.: List of original ICs and replacement parts for the so-called phasebox, attached directly to the vacuum chamber. These are necessary, as some of the original ones are no longer available.

3. Measurements and results

For hydrogen and helium, the ions most prominent in the solar wind [11], angular dependent sputtering yield measurements on the analogue material wollastonite were performed, using the QCM technique. Therefore, wollastonite was deposited on such microbalances by M. Doppler at the Institute of Chemical Technologies and Analytics at the TU Wien and then irradiated using the SOPHIE ion source. This allows to determine sputtering yields for ions with their respective solar wind energies. The results one gets from such measurements allow improvement of calculation of the total sputtering of solar wind ions using BCA simulations [6].

Additionally, a possible charging up of the insulating $CaSiO_3$ layer was investigated using different approaches. Such charging up might be the explanation of a decreasing sputtering for Ar^{8+} with increasing angles of incidence, compared to lower charge states, observed during previous, unpublished measurements. Hydrogen irradiations were performed using various current densities and while flooding the experimental chamber with electrons, keeping the target neutralized. This electron flooding was also used during argon irradiations, comparing the results with and without the gun being active. Lastly, the bulk wollastonite sample was irradiated under both conditions, comparing the results gained at the C-QCM.

3.1. Analysis of the wollastonite mineral and the QCM

For performing typical sputtering measurements using a QCM, target material has to be deposited on a quartz crystal. During this thesis, two different quartzes were used, which were not prepared at the same times, but from the same wollastonite sample. The technique used was Pulsed Laser Deposition (PLD), since it allows the reproducing of the correct stoichiometry even for complex oxides [27]. During both deposition processes, dummy plates made of silicon were placed next to the quartzes and covered as well. Since silicon is part of wollastonite, the plate used in the second batch was gold coated silicon. This way, the target layer could be better distinguished from the base material, when performing depth dependent composition analysis.

Dummy plates from both batches were analysed using X-ray Photoelectron Spectroscopy

(XPS), determining their composition. Furthermore, after irradiation, the target quartz from the first batch was also analysed using sputter-XPS. In this technique, material is removed in layers via sputtering with 3 keV Ar^+ ions, followed by XPS analysis. This way one can in principle get the depth dependent target composition. Difficulties are, that the depth has to be estimated via sputtering rate and duration of irradiation while having changing composition due to preferential sputtering. Using experimental values for the mass removal rate of argon y_{Ar} from [12], one can assume a layer thickness of roughly 50 nm. Not only were deposited layers analysed, but also the wollastonite base material. It therefore was ground and placed on Indium-foil, giving a signal in the XPS analysis, which can be distinguished and filtered out, since there is no Indium in the sample. Results of all composition analyses are shown in table figure 3.1.
The angular dependency of the sputtering yield is not only effected by the target composition, but also by its surface structure [34]. Flat samples have a very distinct angular dependence, whereas this is smoothed out for rough ones. As the bulk sample was placed in the experimental chamber, another piece of wollastonite was prepared in the same way, described in section 2.2.2. Surface analysis was performed using an atomic force microscope by D. Mayer and can be seen in figure 3.2. The mean surface roughness is 3.2 nm, which means that the sample is very smooth, since in this regime effects on the angular dependence of the sputtering yield are typically not present [35].

Comp	rel. [%]			
	Dummy 1	Dummy 2	QCM 1	Original material
O	53.1	61.3	54.2	45.4
C	18.5	6.4	14.6	19.7
Si	16.0	18.7	17.1	13.9
Ca	12.4	12.5	12.2	15.5
N	0	0	0	5.5

Table 3.1.: Target compositions of the dummy plates coated together with the quartzes for both batches, the first target quartz and the original material used for pulsed laser deposition itself, obtained with XPS.

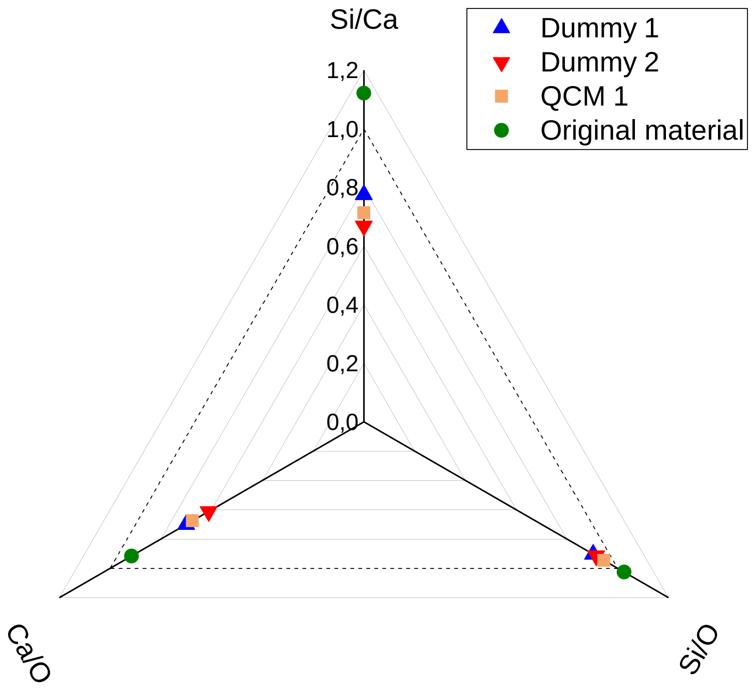

Figure 3.1.: Ratios of the compositions for the three components of wollastonite calcium, silicon and oxygen, normalized to the nominal ones. When comparing the original material with the deposited layers, it is notable that calcium is not redeposited as good as the other two components during the PLD procedure, being under represented in samples of both batches.

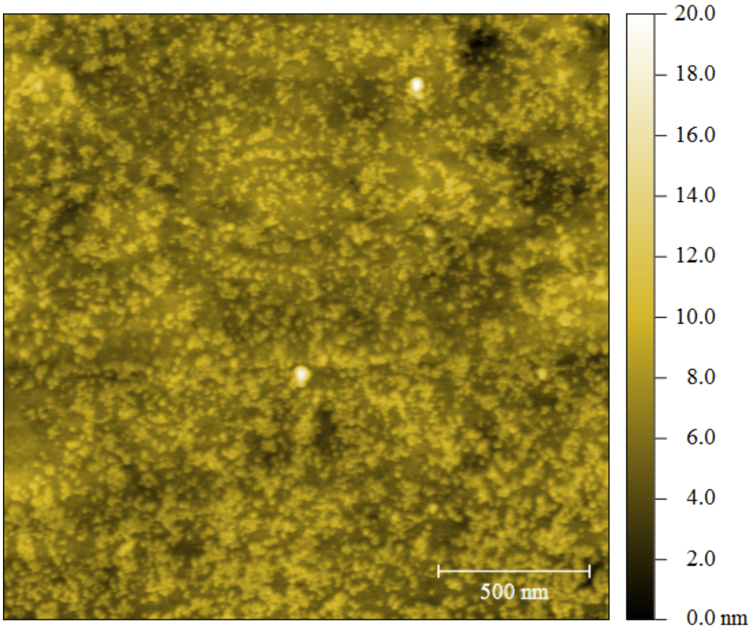

Figure 3.2.: AFM image of a wollastonite sample, which was prepared in the same way as the bulk piece placed in the experimental chamber. Its RMS roughness is only 3.2 nm.

3.2. Hydrogen as projectile

As mentioned in chapter 1, protons make up more than 90% of solar wind ions and an investigation of its sputter yield on analogue materials is of major interest. Therefore, experiments using protons with solar wind energies of 1 keV were favourable. Due to the small currents achieved using the SOPHIE ECR ion source and the small sputtering yield expected for protons, an irradiation of $CaSiO_3$ coated quartzes with protons did have a unfavourably low signal. For molecular hydrogen ions, however, the currents reached were much bigger and in addition with the doubled number of protons per charge gave rise to even higher signals. Thus, measurements were conducted using hydrogen molecules with an energy of 2 keV, which is equivalent to 1 keV per proton. This substitution could be made, since the hydrogen binding energy is 4.5 eV [36] and therefore only a fraction of the kinetic energy. In such a case, the bonds are broken at the first impact on the target, and the two projectiles have different independent collision cascades in the material. In order to determine the total sputtering yield of hydrogen, its angular dependence was investigated. The angle of incidence was varied via turning the target manipulator with respect to the incoming ion beam. In principle, the target holder allows angles of up to 70 degrees, but these were not reachable during some experiments due to the length of the cables and contact issues, which are hard to resolve while the chamber is closed. After one series of measurements, the quartz had to replaced with another one, since the wollastonite layer was worn. Therefore a second series could be obtained, verifying the results of the first one. Figure 3.3 shows the outcome of these for both targets. The small discrepancy can be explained by the fact, that both quartzes come from different batches of deposition, and their layers were deposited at different times, resulting in slightly varying stoichiometry. XPS-analysis of the worn quartz and dummy plates for both batches were done by M. Sauer at the Analytical Instrumentation Center at the TU Wien, showing these slightly different compositions (see 3.1).

Comparing the angular dependent mass removal rates for both target batches show a good agreement. Differences of about 20% can be explained by the slightly different target compositions. Results from the BCA simulations SDTrimSP [19] and SRIM [9] are presented as well. These are used for calculating kinetic sputtering effects and can reproduce the obtained mass removal rate very well for normal incidence. When going to bigger angles however, both overestimate the sputtering effects by more than 50% at

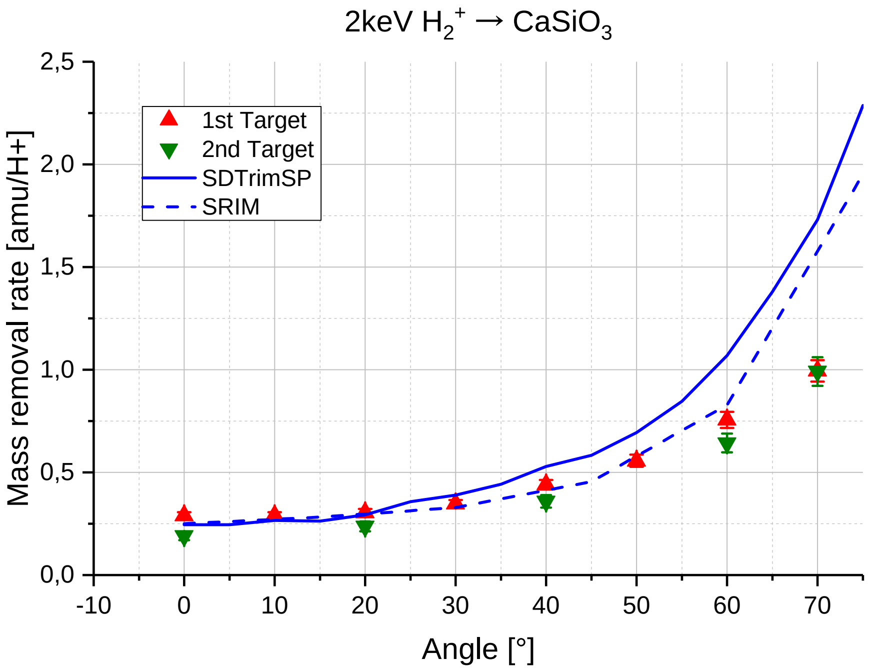

Figure 3.3.: Angular dependent sputtering yield for atomic hydrogen on $CaSiO_3$ with an kinetic energy of 1 keV, obtained using H_2^+ at 2 keV as projectiles. Two different quartzes were used, with their target layers being deposited at different times. The blue lines represents results from BCA simulations performed using SDTrimSP [19] and SRIM [9].

70°. An explanations for this could be the implantation of hydrogen in the wollastonite layer, suppressing the mass removal rate due to sputtering of these light atoms. Other reasons might be chemical effects or even non-linearities due to the usage of molecular hydrogen (see discussion in [12]).

3.3. Helium 4 as projectile

Helium makes up only a small fraction of solar wind, but Szabo et al. suggest, that its contribution to the total sputtering yield is quite significant [12]. This results not from kinetic, but from potential sputtering by He^{2+}, which is the charge state of helium present in solar wind. This conclusion is drawn from measurements performed using argon ions with different charge states with a fixed kinetic energy of 8 keV and a wollastonite coated QCM. The kinetic part of the sputtering yield is gained from SDTrimSP simulations, which reproduces Ar^{+} results very well [12]. After subtracting this quantity, least square fitting the formula $\alpha \cdot \epsilon^{\beta}$ [13] to the gained data, gives the parameters $\alpha = 26.88$ and $\beta = 0.35$, whereas ϵ represents the potential energy of the ions minus two times the material's band gap, which is 5.4 eV for wollastonite. This comes from the idea, that potential sputtering is not possible below this "threshold" energy. As the contribution of potential sputtering is only depending on the potential energy of the impinging ions, this formula can in principle also be applied for helium [12]. Doing so, gives rise to a significant increase from 2.55 $^{amu}/_{ion}$ to 12.92 $^{amu}/_{ion}$ for the expected sputtering yield of He^{2+} compared to He^{+} under normal incidence. Therefore, the contribution of helium to the total sputtering yield of solar wind ions also increases significantly to about 65% [12].

Since the kinetic fraction of the helium yield was here based on the outcome of BCA simulations, irradiations were first performed using $^{4}He^{+}$ as projectiles in order to verify this assumption. These results can later be used to separate the kinetic and the potential contribution to the total sputtering yield of $^{4}He^{2+}$.

As mentioned before, solar wind energies are typically 1 $^{keV}/_{amu}$, which requires an acceleration voltage of 2 kV for $^{4}He^{2+}$ and 4 kV for irradiations with $^{4}He^{+}$. These two charge states are well separable with the dipole magnet, which has a $^{m}/_{q}$ dependent deflection. Also, with this ratio being 4 for the singly ionized helium, a contamination with different ions is very unlikely, as high charge states would be needed. For $^{4}He^{2+}$ however, this is a serious problem, since ionized hydrogen H_2^{+} molecules and $^{4}He^{2+}$ both have a mass over charge ratio of 2. As hydrogen is difficult to pump using turbo molecular pumps, as they are used in the SOPHIE, it will always be present to some degree in the residual gas. This gives rise to a quite significant uncertainty in the sputtering yield of $^{4}He^{2+}$, as the expected yield differs by a factor of 35 at 0° between these two projectiles, while both account to the current measured. This effect on the calculated yield is doubled by the fact that the helium is doubly charged, increasing this ratio to about 70. Thus, even small fractions of hydrogen in the ion beam have a significant effect on the measurement.

For the conducted measurements, a QCM target from batch 2 was irradiated with 4 keV He^+ and He^{2+}. Results of the obtained angular dependent sputtering yield are presented in figure 3.4. The error bars there include an additional uncertainty due to contamination with hydrogen, which is added to the usual measurement uncertainty. Here, 10% of the current is assumed to be H_2^+ ions, with their mass removal rate taken from section 3.2, where y_{H_2} was divided by a factor of 2 in order to get y_H. Assuming independent sputtering for both ions, the beam current would have to consist of 83% hydrogen, if the mass removal rate of He^{2+} would be 12.92 amu/ion for normal incidence. Due to currents of some 100 nA of the focused ion beam at the faraday cup, this amount of hydrogen contamination can most likely be excluded. The mass removal rate due to potential sputtering of He^{2+} might therefore be smaller than expected. Another explanation could be a suppression of the observed mass removal due to implantation and sputtering of the light hydrogen molecules, leading to non-linear dependency on the hydrogen content in the beam.

For He^+ however, the SDTrimSP results match the experimental values very well. It is therefore able to reproduce the kinetic sputtering of helium on a $CaSiO_3$ target.

In the following, the deviation from the calculated mass removal rate y_{calc} for $^4He^{2+}$ ions due to hydrogen contamination is derived, based on equation 1.4 in section 1.3. It is considered here, that sputtering for both projectiles is independent. Therefore, the frequency changes due to each sort of ions can be added up. The C_i consist of constants independent of the projectiles and the inverse charge state of the ions.

$$y_i = \left(\frac{\Delta f}{\Delta t}\right)_i \cdot \frac{C_i}{j_i} \tag{3.1}$$

$$j = j_{He} + j_{H_2} \tag{3.2}$$

$$y_{calc} = \frac{\Delta f}{\Delta t} \cdot \frac{C_{He}}{j} \tag{3.3}$$

$$\frac{\Delta f}{\Delta t} = \left(\frac{\Delta f}{\Delta t}\right)_{He} + \left(\frac{\Delta f}{\Delta t}\right)_{H_2} = \frac{y_{He} \cdot j_{He}}{C_{He}} + \frac{y_{H_2} \cdot j_{H_2}}{C_{H_2}} \tag{3.4}$$

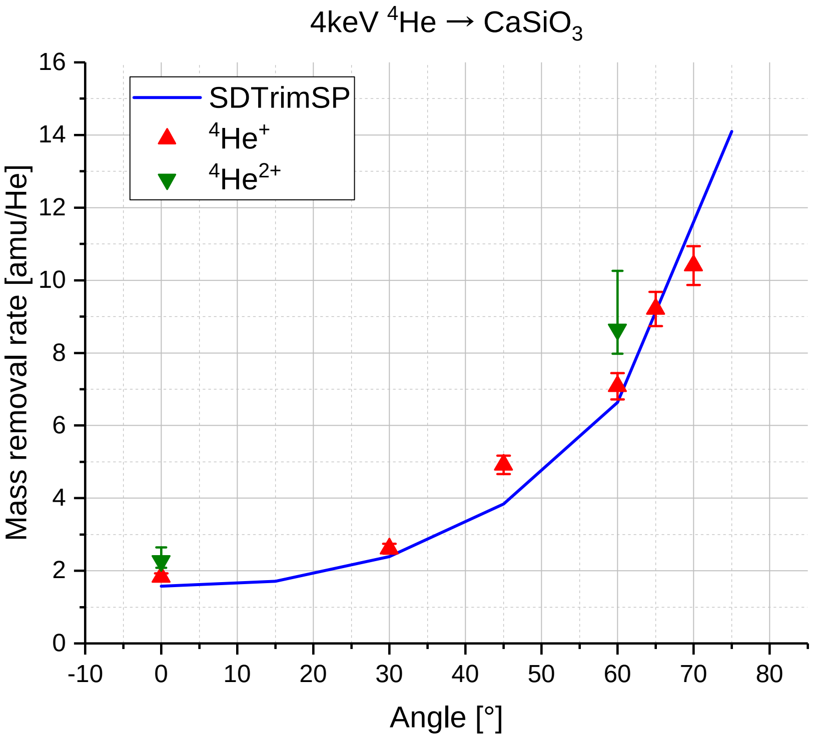

Figure 3.4.: Mass removal rate in dependence of angle of incidence for ^{4}He$^+$ and ^{4}He^{2+} with a kinetic energy of 4 keV on a CaSiO$_3$ target. The error bars for ^{4}He^{2+} represent 10% molecular hydrogen in the ion current, as H_2^+ cannot be separated from ^{4}He^{2+} using the dipole magnet. The blue line represents results from SDTrimSP, which only takes into account kinetic sputtering.

$$\Rightarrow y_{calc} = \frac{C_{He} \cdot \frac{y_{He} \cdot j_{He}}{C_{He}} + \frac{y_{H_2} \cdot j_{H_2}}{C_{H_2}}}{j_{He} + j_{H_2}} \tag{3.5}$$

$$\Rightarrow y_{He} = \frac{y_{calc} \cdot j - \frac{C_{He}}{C_{H_2}} \cdot y_{H_2} \cdot j_{H_2}}{j_{He}} \tag{3.6}$$

Assuming a contamination of the current with 10% hydrogen molecules:

$$j_{He} = 0.9 \cdot j \tag{3.7a}$$

$$j_{H_2} = 0.1 \cdot j \tag{3.7b}$$

$$\Rightarrow y_{He} = \frac{y_{calc} - \frac{C_{He}}{C_{H_2}} \cdot y_{H_2} \cdot 0.1}{0.9} = \frac{y_{calc} - 0.05 \cdot y_{H_2}}{0.9} \tag{3.8}$$

With $\frac{C_{He}}{C_{H_2}} = 0.5$ due to the different charge states of $^4He^{2+}$ and H_2^+. The deviation between the calculated mass removal rate y_{calc} of helium excluding contaminations in the ion current and y_{He}, which takes them into account is therefore mainly determined by the increased measured current. This is valid for small fractions of hydrogen in the beam and independent sputtering for both projectiles, as it was assumed during this derivation.

In addition to 4 keV helium ions, irradiation with kinetic energies of 1 keV and 2 keV were performed with singly charged helium 4. In figure 3.5, both angular dependent mass removal rates are shown together with results from SDTrimSP, where the targets composition from XPS analysis was used. It can be seen, that these reproduce the experimental results very well, being within the measurement uncertainty for almost all points measured.

3.4. Charging up of the QCM

As mentioned above, some measurements using argon showed a decreasing sputtering yield for increasing charge states at gracing incident. Possible explanations for this behaviour are a charging up of the wollastonite layer, which is non-conductive, or angular dependent potential sputtering, which could not yet be observed [10]. Therefore, an electron flood gun was attached to the experimental chamber, delivering electrons to keep the target neutralized. Although the ejected electrons are not pointing directly to the targets (see section 2.2), it should nevertheless be able to keep the target neutral, as electrons have a fairly high backscattering rate [31]. In order to verify its performance, various tests were conducted, such as current measurements at the target faraday cup and variation of emission current.

Analysis of charging up was performed in several ways, such as the variation of ion and electron current as well as measurements using the catcher setup and a bulk wollastonite target. The combination of bulk material irradiation and different electron supply can

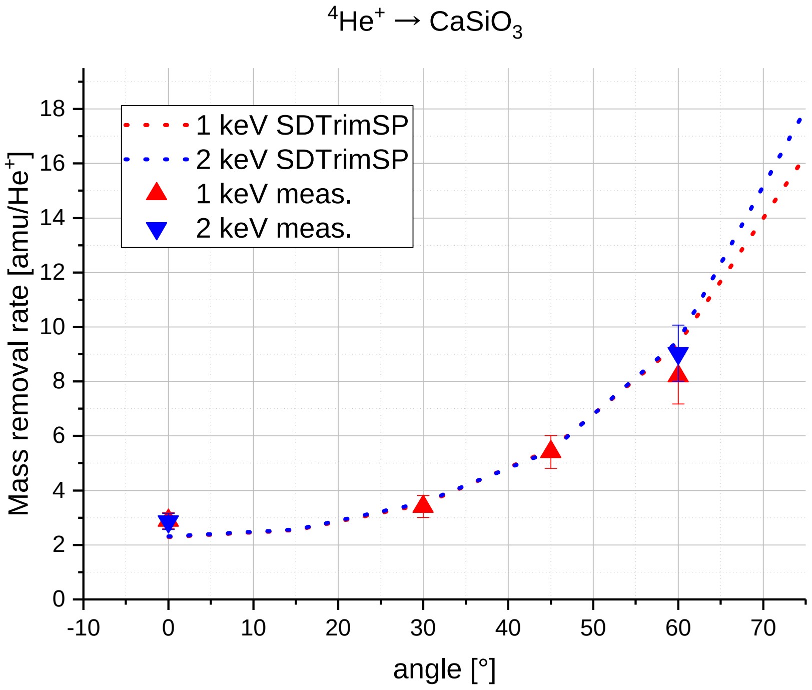

Figure 3.5.: Angular dependent mass removal rate for $^4He^+$ ions on $CaSiO_3$ for energies of 1 keV and 2 keV from measurements and SDTrimSP. The results for both energies are very similar, with simulation curves for both energies coinciding for a wide range of angles.

give a qualitative guideline for the charging up of the layer deposited on the quartz, as it can give an upper limit for the influence of charging up and neutralisation.

3.4.1. Ion current variation using hydrogen

Since the voltage building up is depending on the current density as described in section 3.4, a variation of this can be used for determining a charging up effect. A currents achieved with hydrogen molecules are an order of magnitude bigger as for Ar^{8+}, a charging up should be observable here as well. Therefore, first measurements to test the charging up behaviour were obtained using H_2^+ ions with several different current densities. For these, the angle of incidence was set to 60 degree, where a charging up should have a visible effect on the QCM signal. The scanned current measured at the

0.6 mm^2 faraday cup and thus the effective current density was varied by almost a factor of three, with currents going from about 2000 pA to 6000 pA in a first series. It later was increased to up to 12500 pA in a series performed when comparing signals with and without the flood gun, which is discussed in section 3.4.3. Mass removal rates depending on the ion current obtained during both series are shown in figure 3.6. Overall there is no trend due to variation of ion current observable in the signal. However, as the mass removal rate has a distinct angular dependence at about 60° and increases more than 20% when going to 70° (see section 3.2), charging up can not be completely ruled out by this test alone. For a charged up sample, the average angle of incidence will be different as for a neutral one, as also the ions hitting the surface will be deflected to some degree. If the mean angle of incidence increases, the bigger sputtering yield for higher angles can compensate for the ions missing the surface at all. Therefore, other testing on a charging up of the sample had to be performed, such as those using the electron flood gun, described below. There is also a scattering in the data presented in figure 3.6 of about 35%. This might be explained due to beam stability and long irradiation times needed. Another possible reason might be contaminations of the surface, also having an influence on the signal for longer times due to the small mass removal rate of hydrogen.

3.4.2. Testing the flood gun without ion beam

Due to the positioning of the flood gun (see section 2.2), it had to be verified, that a sufficient amount of electrons can be delivered to the target. For this purpose, the current at the faraday cup was measured without an ion beam but with the flood gun turned on. As lenses and deflection plates for guiding of the electron beam are available, these were used in order to maximize the current. The effect of these however was only in the range of 10% and were kept constant after the first adjustment. The two adjustments changing the number of electrons hitting the faraday cup significantly were the energy of the emitted electrons and the grid potential. As mentioned in 2.2.2, the maximum in current was found for an emission energy of about 30 eV with an grid potential of zero volts. Since the current was fluctuating a lot, this varied from about 1 nA to 100 nA, but was in the range of 1nA to 5nA during most of the measurements. Figure 3.7a shows such a current measured at the faraday cup, with the grid potential varied in steps over time. One can see, the signal is very noisy for the highest currents, corresponding to 0 V Grid

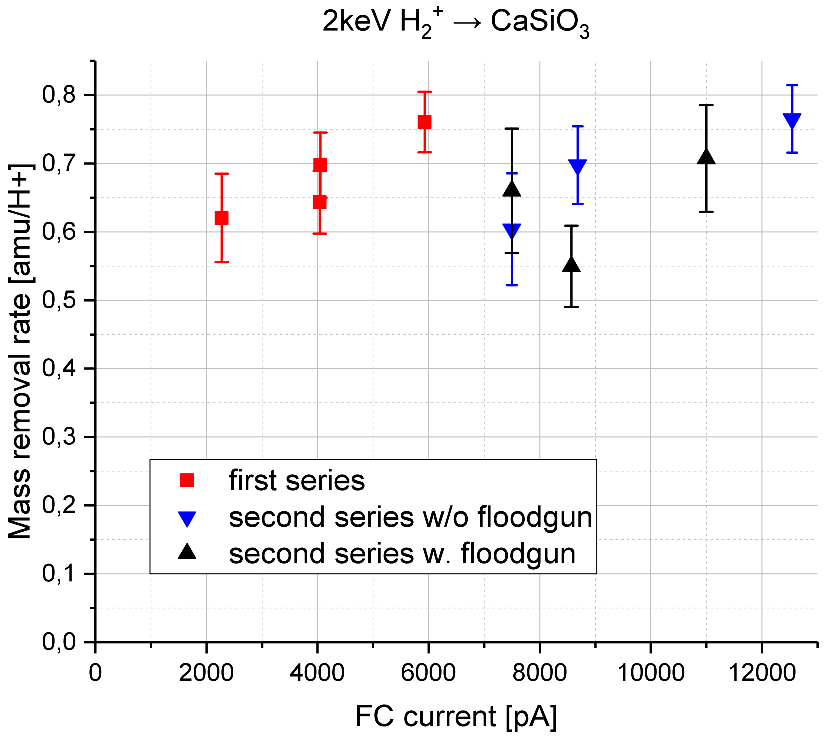

Figure 3.6.: Ion current density depending sputtering yield for hydrogen molecules under under an angle of 60° and with an energy of 2 keV, including measurements with the electron flood gun turned on. Neither a current dependency nor one of the electron emission can be found, indicating that the target is not charging up.

potential. A further test of electron supply for charging up targets was performed using a battery and a potentiometer, putting the faraday cup on a variable potential. This was varied stepwise from 0 V to 47 V and back down every 100 s, while logging the current using a PC. Figure 3.7b shows the mean values at the cup for these steps. It can be seen, that current measured increases with the applied voltage as one would expect. A charging up target would therefore attract more electrons, still keeping it neutral.

It has to be mentioned, that the faraday cup line is not shielded or insulated completely on the back side, and therefore electrons are detected outside of the actual cup. Figure 2.6 in section 2.2.2 shows the back side of the target holder as it is mounted in the experimental chamber. One can see, that connectors make up most of the faraday cup area there, as the mounting is insulated with Teflon tape. As a turning off of the faraday cup suppressing voltage, which is about 40 V and therefore more than the electrons kinetic energy, only changed the current measured by about 10%, most of their detection happens at the back side. The effective area can be estimated to be in the same order as the irradiated quartz surface, which is more than 50 mm^2 when using the 4 mm aperture and irradiating under an angle of 60°. As mentioned above, this diameter was usually used for measurements on the QCM target, as the majority of the sensitive quartz is still covered for 0° and the error therefore negligible.

During measurements with Ar$^+$ ions, currents were usually in the range of 10-20 nA and even lower for more highly charged ions, which is still bigger than the typical current measured for the flood gun. Considering however the significant rise in electron current for increasing voltages at the faraday cup, one can assume, that the supply of electrons is enough to guarantee a neutralization of the target. Also, as mentioned later in section 3.5, changes in the emitted electron current by one order of magnitude did not affect the catcher signal at all for irradiations of the bulk sample. This indicates, that the supply of electrons is more than enough. Otherwise, the voltage building up on the target would vary with the electron current, leading to changing sputtering yield and catcher signals.

3.4.3. Testing the flood gun using ion beams

The quartz crystal microbalance is a very sensitive tool, which reacts notably to all kinds of external stimuli. Small changes in temperature for example lead to a significant drift of the resonance frequency. It was therefore important, that the presence of an electron

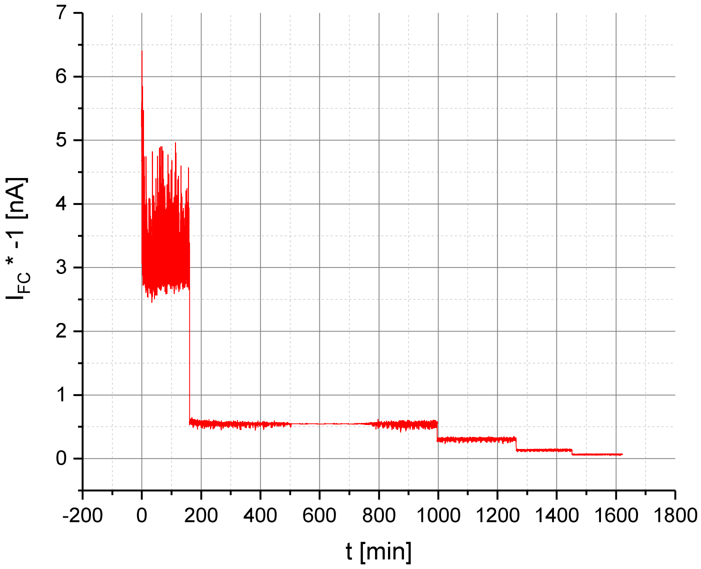

(a) Current measured at the faraday cup for a variation of grid potential at the electron flood gun and a constant energy of 30 eV.

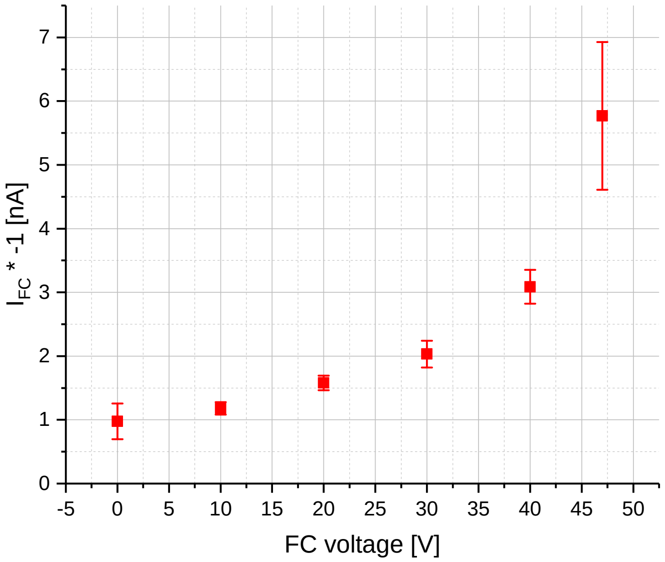

(b) Electronic current at the faraday cup for different cup potentials. This was varied using batteries and a potentiometer, while flood gun parameters were kept constant.

Figure 3.7.: Currents measured at the faraday cup for different scenarios.

flood gun does not influence the measurements in a negative way. As mentioned in 2.2.2, during the first test after installation, the pressure in the target chamber increased by one order of magnitude when the filament was turned on. A further increase happened when the extraction voltage was turned on as well. There were also effects on the QCM visible, with the signal becoming more noisy and the drift getting bigger when using the electron gun. It changed from $0.1\ ^{\mathrm{mHz}}/_{\mathrm{min}}$ to $1\ ^{\mathrm{mHz}}/_{\mathrm{min}}$, which is still smaller than the estimated uncertainty used typically for the data obtained of $3\ ^{\mathrm{mHz}}/_{\mathrm{min}}$. After about two weeks, the increase in pressure when turning on the filament got barely notable, and also the effect on the quartz signal when turning on electron emission was vanished. Therefore measurements using the flood gun could be performed just as without it.

As already mentioned in section 3.2, hydrogen irradiations with active electron gun were performed, also for different ion currents. These did not reveal any neutralisation effect on the target layer (see figure 3.6), thus showing no charging up. Further tests were obtained using argon ions, which is especially interesting for Ar^{8+}, because measurements performed with these ions indicate a charging up of the quartz crystal. As representing the extreme cases, irradiations using Ar^{+} and Ar^{8+} were performed. As most reference data existed for 2 keV for singly charged argon and 8 keV for Ar^{8+}, these energies were chosen. Similar to hydrogen, measurements were performed under an angle of 60° and compared between with and without electron supply, as well as to existing data. Results of these are shown in figure 3.8.

As well as for hydrogen irradiation, no effect of the electron gun was observable, strengthening the conclusion, that a charging up of the non-conductive target layer does not take place. As the angular dependency of the argon sputtering yield is much less prominent than for hydrogen [12], it would be very surprising, if changes in the angle of incidence would compensate here as well as for hydrogen.

Nevertheless, in addition to testing charging up with the electron gun using the target QCM, measurements using the wollastonite bulk target and the catcher setup were performed. The signal of the C-QCM is not only sensitive to the total sputtering yield, but also to the position where target particles are emitted from and their angular distribu-

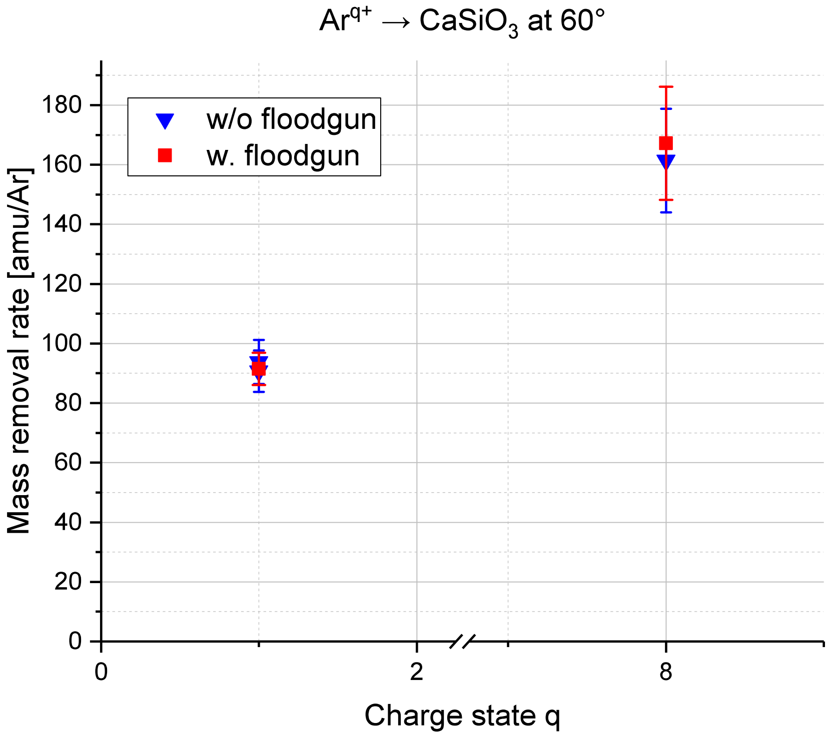

Figure 3.8.: Results of target irradiation with 2 keV Ar^+ and 8 keV Ar^{8+}, both under an angle of incidence of 60°. For each settings, one data point is obtained with, and one without electron supply being active. No difference in the obtained data can be seen for both cases for either of both projectiles.

tion. A charged up sample deflecting the ion beam would at least cause such a variation, which should be observable in the signal. During this measurements, the electron gun was not only turned off or on, but the emission current was also varied via the grid potential. A qualitative observation of the available electrons was made as in the tests in section 3.4.2, where these were measured using the faraday cup and a picoamperemeter. The current was logged during the irradiation phase, allowing a direct comparison of electron supply and quartz signal.

Due to air condition related oscillations in the room temperature, the drift of the catcher quartz was varying over time with a period of approximately one hour and a slope of up to $6\,\mathrm{mHz/min}$. This is challenging, since signals of the C-QCM are only in the range of $10\,\mathrm{mHz/min}$ during irradiation. Due to the periodicity of temperature variations, measurements performed over several hours still allow drawing conclusions about the effect of electron supply on the sputtering related quartz signal. Figure 3.9 shows the temperature drift for several hours without irradiation, the linear fit shown there has a slope of less than $0.1\,\mathrm{mHz/min}$.

While variations in the emission current of the electron gun did not affect the signal obtained at the C-QCM, a complete turning off of the electron supply was observable in the signal. Figure 3.10a shows such a catcher signal, while it was irradiated with and without the electron gun active. A Savitzky-Golay-filter with a length of 50 values and 5 iterations was applied in order to get information over the local slopes in figure 3.10b. The respective phases corresponding to irradiations of the mineral and active electron gun are noted in both graphs. One can see, that the local slopes differ between the phases where the electron gun was active and not. Since no change in signal is observed when the electron gun is active but the ion beam is not, this effect can be linked to changes in the sputtering process occurring at the bulk target. Mean slopes for the phases are shown in figure 3.11. The visible variation in QCM-Signal due to neutralisation is between 20 and 30% and independent of emission current, which means that even a small fraction of the maximal available electrons are sufficient for neutralizing the target completely.

As the observable effect is fairly low with the insulating bulk target, the conclusion is strengthened, that there is no charging up taking place for the QCM target, as the deposited layer there is maximal some hundred nanometre thick. Neutralization via electrons from the metal surface below surely is faster for the QCM layer, as in the case

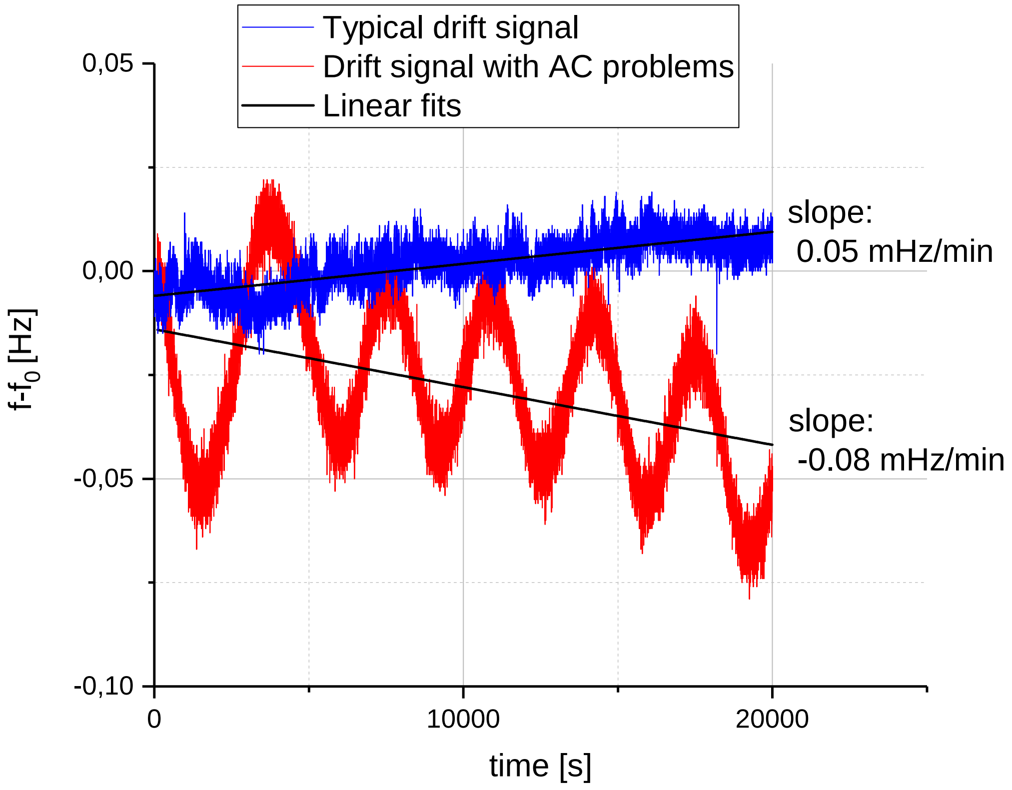

Figure 3.9.: Frequency of the catcher quartz for several hours without irradiation when oscillations in the lab temperature due to the air conditioning were present and not. These oscillations could be smoothed by increasing the phasebox mass, keeping it at a more constant temperature.

of the bulk target. Here, neutralization most likely happens due to surface conductivity. Even if this is significantly better per distance as through the bulk, distances to the electrodes are several orders of magnitude bigger, as the deposited layer is surely much thinner than 1 μm and distances from the centre of the bulk to the front plate are several millimetres.

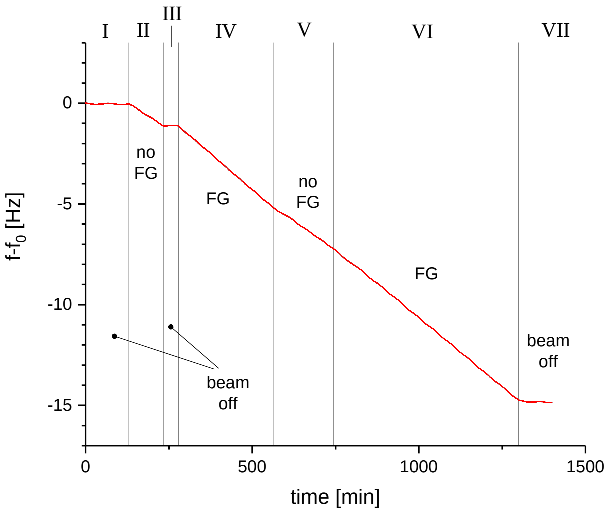

(a) Signal at the C-QCM during irradiation of the wollastonite mineral with phases having the flood gun (FG) on and off.

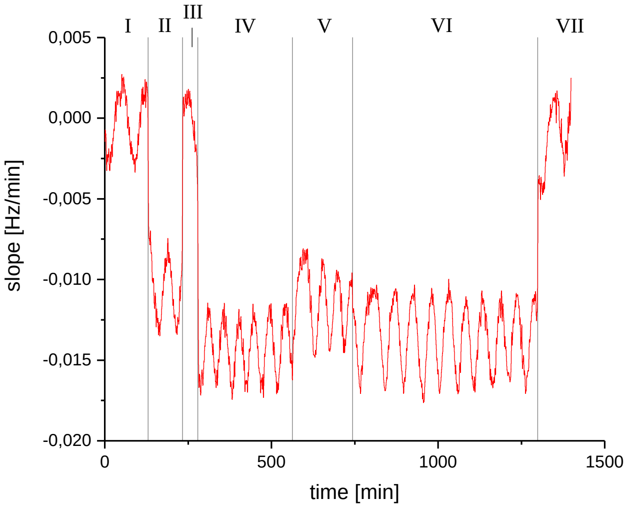

(b) Local slope of the C-QCM signal during the irradiation, obtained using a Savitzky-Golay-filter with a length of 50 values and 5 iterations.

Figure 3.10.: Signal and resulting local slope of the catcher QCM for irradiation of the wollastonite mineral with 2 keV Ar$^+$ under an angle of 60°. The 2 mm aperture was used and the scanned current at the faraday cup was 900 pA. Flood gun settings were such that maximal current was achieved in the faraday cup. There was no irradiation during phases I, III and VII, irradiation without electron emission from the flood gun in phases II and V and irradiation with electrons in phases IV and VI.

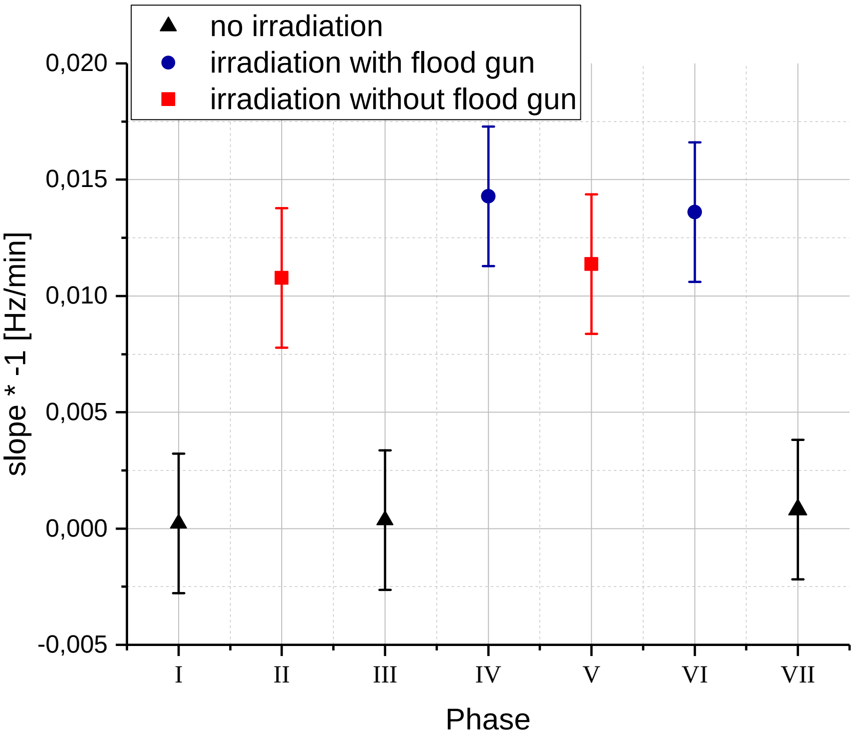

Figure 3.11.: Mean slopes for each phase of the mineral irradiation, with and without flood gun emission active. Both times electrons were emitted, the signal increased for roughly 20%.

3.5. Catcher measurements with a wollastonite target

Direct comparisons of both, the QCM and the bulk target were performed, via moving the sample holder up and down during one irradiation. This is advantageous for measurements at the C-QCM, since signals there are only in the range of a few $^{\mathrm{mHz}}/_{\mathrm{min}}$ and therefore much smaller than at the target QCM. Undesired effects such as temperature induced drifts are very similar for both targets when the irradiations are performed directly after each other, allowing for better comparison of them. Figure 3.12 shows the signals obtained at the C-QCM for such a measurement cycle. A downside of this technique is the small slope of the frequency decrease, as only a fraction of the sputtered particles hits the catcher. The signals are therefore much more sensitive to thermal drifts taking place without irradiation. These are mainly related to changes of the phasebox temperature and squeezing it between two aluminium plates reduced the response in the quartz signal to changes of the ambient temperature and improved the quality of catcher measurements, which is also shown in figure 3.12, comparing signals for both cases.

In order to get information about the different distribution of sputtered particles for both bulk and QCM sample, the target holder was moved along beam direction for several angles of incidence. For these positions, the sector of the angular distribution covered by the catcher is changing. The ratio of the signal there can therefore give information about the distribution of sputtered particles for both targets.

Although ion currents achievable are much bigger for hydrogen, measurements were performed using Ar^+ ions, as the much higher sputtering yield more than compensates for the smaller currents. Furthermore, kinetic sputtering on $CaSiO_3$ targets is very well reproducible for argon with SDTrimSP . It therefore was favourable to use these ions instead of hydrogen, where the alignment is not that good.

As for most of the irradiation sequences, signals were not only taken when the ion beam is impinging, but also in beam off phases. During these, the drift of the quartz frequency can be determined and an average subtracted from the one during irradiation. This technique is however limited, as the drift can change during irradiation. Nevertheless, drastic changes in this drift which affect the signal are typically visible there and can also be taken into account. In this cases, the uncertainty is assumed to be bigger as for irradiations with constant drift. To compare the signals for both targets, the ratio of

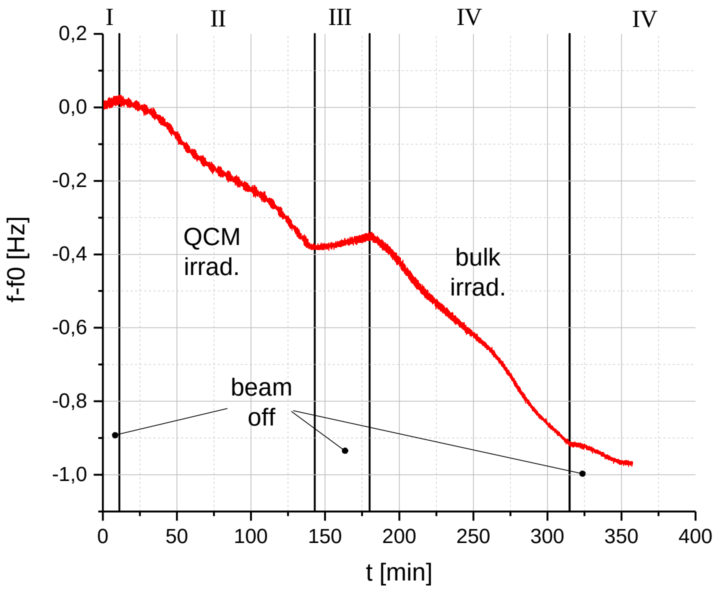

(a) Signal at the catcher when irradiating both the QCM and the bulk target taken without the additional mass at the phasebox

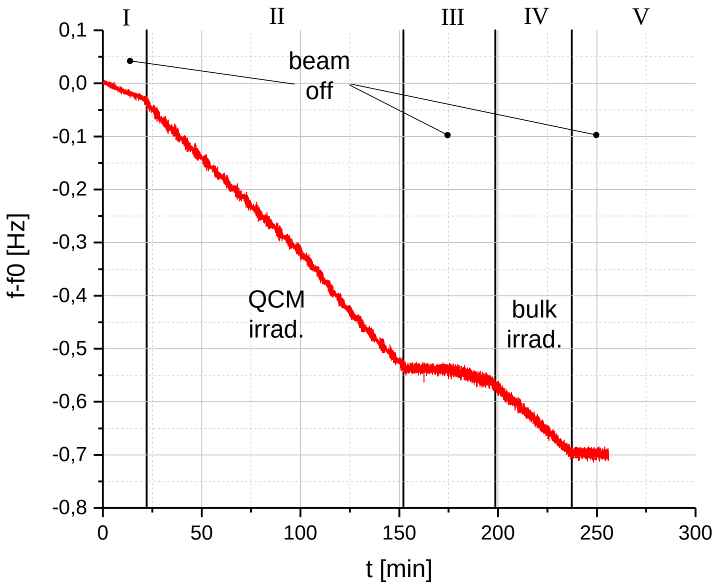

(b) Catcher signal with the buffering plates mounted to the phasebox

Figure 3.12.: Comparing of the signal at the C-QCM with and without increased phasebox mass and therefore thermal buffering. During phases I, III and V no irradiation is performed, II and IV are QCM and bulk sample irradiation.

them is calculated and shown in figure 3.13. It has to be noted, that uncertainties must not be neglected here, but are difficult to quantify due to varying circumstances. However, the trends observed still hold, as the QCM and the mineral were always irradiated directly after each other. One can clearly see, that the signal obtained for the bulk target is significantly smaller than the one for the deposited layer for all angles of incidence. The ratio of these signals goes down from about 0.9 at 60° to 0.3 at 40°. This leads to the conclusion, that the total sputtering yield for the wollastonite mineral is much smaller than for the $CaSiO_3$ layer deposited on the target quartz. Additionally, a reduction of the signal ratio towards smaller angles of incidence can be seen. A possible explanation for this trend could be, that the angular distribution of sputtered particles is different. The expected catcher signal was calculated for several different $\cos^y(\varphi)$ angular distributions of sputtered particles in order to substantiate that theory. Considering a $\cos^8(\varphi)$ distribution for the bulk target and a $\cos(\varphi)$ distribution for the QCM, the trend of a decreasing signal ratio towards smaller angles of incidence can be reproduced. Both distributions are shown in figure 3.14 for angles from zero to $\pi/2$, where it can be seen, that the latter is much broader. When scaling the signal ratio at the catcher calculated for these two distributions by a factor of 0.18, one gets fairly good quantitative agreement with the measurement data (figures 3.13 (b)-(c)). Trends for the variation of target position are not described well here, but discrepancies between model and experiment are within the limits of uncertainty.

The results from the calculations support the hypothesis, that the sputtered material from the mineral firstly gets ejected in a much narrower solid angle and is secondly far less than for the QCM target.

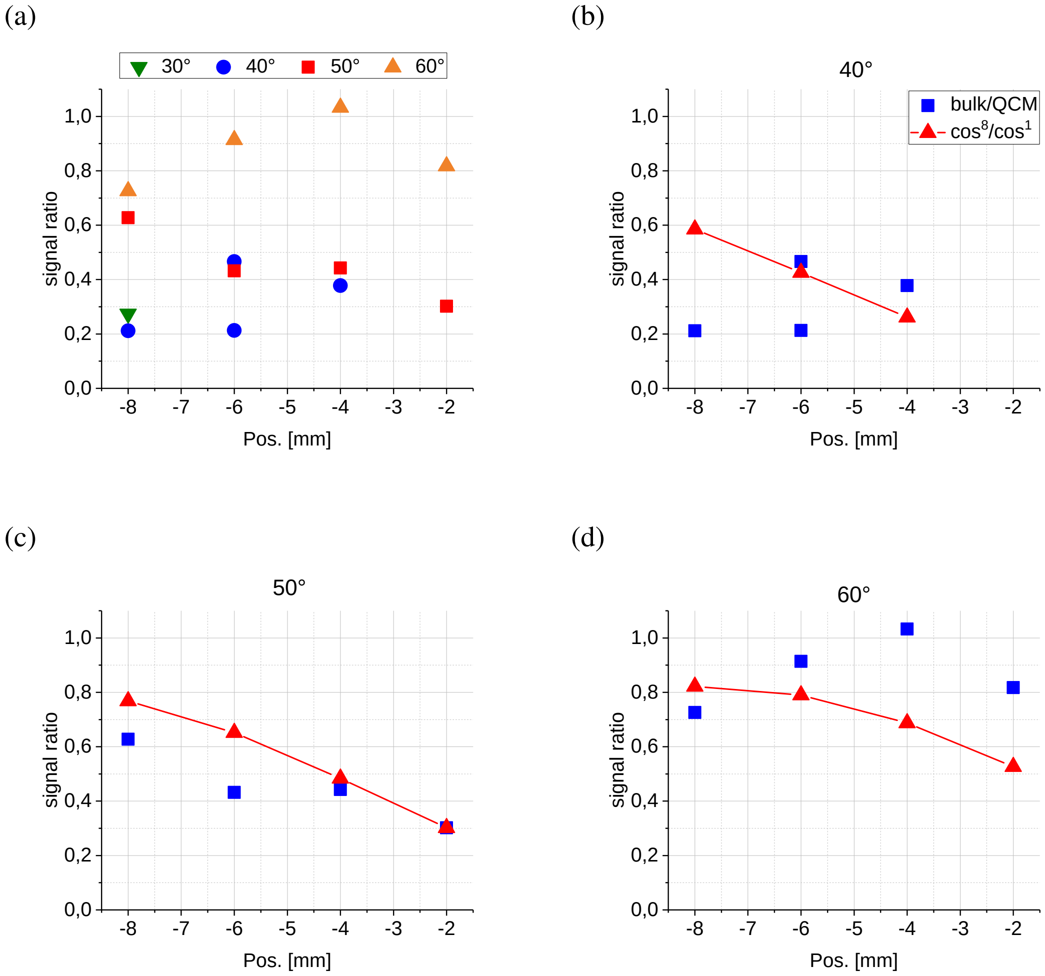

Figure 3.13.: Ratios of the catcher signals for irradiations of both the $CaSiO_3$ layer deposited on the QCM and the bulk wollastonite target at several angles of incidence (sub-figure (a)), together with the ratio one would expect for a $\cos^8(\varphi)$ and a $\cos(\varphi)$ distribution of sputtered particles (sub-figures (b-d)). Simulated ratios are scaled to the value at the -2 mm position under an angle of 50°.

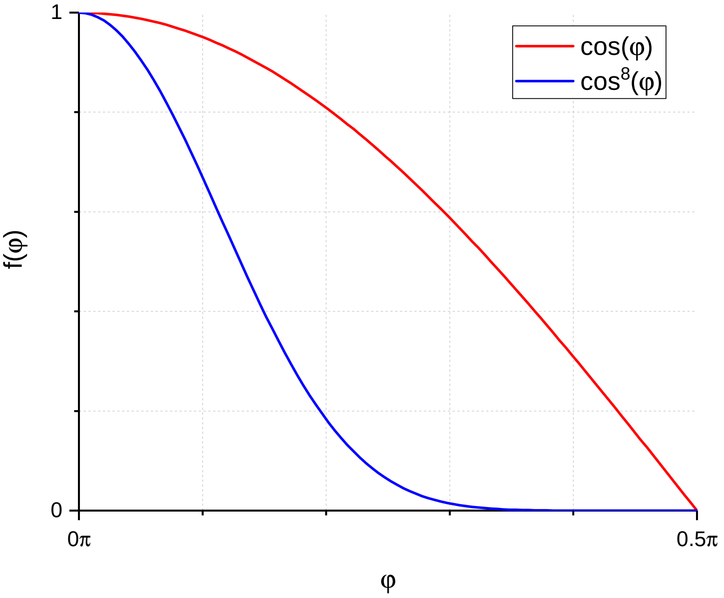

Figure 3.14.: Comparison of a $\cos(\varphi)$ and a $\cos^8(\varphi)$ function, which are used to describe the qualitative difference in the catcher signals for the QCM and the bulk target.

4. Summary

The term space weathering sums up several influences on bodies in space, like thermal desorption, micro meteoroid impact, electromagnetic radiation and solar wind ions. The effect of sputtering due to these ions was investigated during this thesis, using wollastonite ($CaSiO_3$), an analogue material for lunar regolith. As hydrogen and doubly charged helium make up most of solar wind ions, investigations of the angular dependent mass removal rate on $CaSiO_3$ samples were performed with energies of 1 keV/amu. For this purpose, wollastonite was deposited on a quartz crystal microbalance and irradiated using the 14.5 GHz ECR ion source at the Institute of Applied Physics at the TU Wien. This tool allows in situ and real time observation of mass removal of target layers via the change of the quartz resonance frequency.

For hydrogen, two batches of quartzes were irradiated, showing reproducibility of the obtained results. These are also compared to the outcome of BCA simulations using SDTrimSP and SRIM. Both agree well with the experimental data for normal irradiation, but overestimate the mass removal rate for higher angles of incidence. That might be explainable by implantation of hydrogen in the wollastonite layer, chemical effects or even non-linearities due to the usage of molecular hydrogen.

Wollastonite is an insulator, and potential sputtering due to $^4He^{2+}$ is expected to have a major influence on the mass removal. Therefore, measurements were made with both charge states of helium at the same kinetic energy. Because $^4He^{2+}$ cannot be separated from H_2^+ with the dipole magnet used in the setup, contaminations have to be expected here, giving quite significant uncertainty to the results obtained. This problem can be overcome when using $^3He^{2+}$ instead. Nevertheless, the expected value for $^4He^{2+}$ under normal irradiation is 12.92 amu/ion, while the measurements show only 2.27 amu/ion. For explaining this discrepancy with hydrogen contamination alone would lead to a hydrogen amount of 70%, considering independent sputtering of both ions. As currents were in the range of hundreds of nanoamperes, this can probably be excluded. The sputtering of hydrogen itself is however not fully understood yet, and again implantation of hydrogen or chemical effects could lead to non linear dependency on the hydrogen amount in the ion beam.

Results are also compared to the outcome of SDTrimSP simulations, showing good agreement with $^4He^+$ for the whole angular dependency. This indicates, that sputtering here is dominated by the kinetic part. In addition to 4 keV $^4He^+$, measurements were conducted with 1 keV and 2 keV as well, which are also reproduced very well by SDTrimSP simulations.

Additionally to measurements of mass removal rates, a possible charging up of the non-conductive wollastonite targets were was investigated. For this purpose, an electron flood gun was mounted to the experimental chamber, current density variations of the ion beam and irradiations using the so-called catcher setup were performed. The different ion current densities should lead to changes in the calculated mass removal rate, as the voltage building up is dependent on it. These measurements were conducted with hydrogen under an angle of 60° and a current spread by a factor of 6, but no trend in the signal could be observed. The electron gun was in use during some of these irradiations as well, also showing no increase in mass removal rate. Further investigations with the electrons were performed using Argon (Ar^+ and Ar^{8+}) ions. Signals were compared between measurements with and without the electron gun being active, and here no difference was observed either. Using the QCM-catcher setup, it was possible to investigate the effect of the additional electron supply on a bulk wollastonite sample as well. Differences here were only in the range of 20 to 30%, showing good surface conductivity of the wollastonite sample, which was pressed towards a metal plate for clamping. Furthermore, this effect of neutralisation was independent from reducing the number of emitted electrons by an order of magnitude, showing that the supply is more than sufficient to keep both $CaSiO_3$ samples neutral. All in all, an effect due to charging up of the deposited target layer can be excluded. An alternative explanation might be, that the steady state was not yet reached in previous irradiations, and the target surface was still changing due to preferential sputtering. The mass removal rates for Ar^{2-7+} could then also be smaller than expected from earlier results.

Lastly, the catcher setup was used to compare the angular distribution of the sputtered particles for both, the $CaSiO_3$ layer on the QCM target and the bulk wollastonite sample. Theses showed quite significant deviations from each other, when the relative position and angle between targets and catcher were varied. Here, the distribution of sputtered particles seems to be much more narrow for the wollastonite piece. As the ratio between the two catcher signals never exceeded one, the total sputtering yield also has to

be smaller for the mineral sample.
Comparisons with simulations using a $\cos^8(\varphi)$ and a $\cos(\varphi)$ angular distribution of sputtered particles show quite similar behaviour, when scaling the narrower $\cos^8(\varphi)$ distribution by a factor of 0.18. This indicates, that the mineral indeed ejects less material to flatter angles, reducing its total sputtering yield.

Bibliography

[1] Hapke B., "Space weathering from Mercury to the asteroid belt", *Journal of Geophysical Research: Planets*, **106**, 10039 (2001)

[2] Pieters C.M., Taylor L.a., Noble S.K., Keller L.P., Hapke B., Morris R.V., Allen C.C., Mckay D.S. and Wentworth S., "Space weathering on airless bodies: Resolving a mystery with lunar samples", *Meteoritics & Planetary Science*, **35**, 1101 (2000)

[3] Taylor S.R., "CHAPTER 12 - The Moon", in L.A. McFadden, P.R. Weissman and T.V. Johnson, eds., *Encyclopedia of the Solar System (Second Edition)*, 227 – 250, Academic Press, San Diego, second edition edition (2007)

[4] Behrisch R. and Eckstein W., *Sputtering by particle bombardment: experiments and computer calculations from threshold to MeV energies*, Springer Science & Business Media (2007)

[5] Alnussirat S.T., Barghouty A.F., Edmunson J.E., Sabra M.S. and Rickman D.L., "Contributions of solar-wind induced potential sputtering to the lunar surface erosion rate and it's exosphere", *Nuclear Instruments and Methods in Physics Research Section B: Beam Interactions with Materials and Atoms*, **420**, 33 (2018)

[6] Wurz P., Whitby J., Rohner U., Martín-Fernández J., Lammer H. and Kolb C., "Self-consistent modelling of Mercury's exosphere by sputtering, micro-meteorite impact and photon-stimulated desorption", *Planetary and Space Science*, **58**, 1599 (2010)

[7] Vervack R.J., McClintock W.E., Killen R.M., Sprague A.L., Anderson B.J., Burger M.H., Bradley E.T., Mouawad N., Solomon S.C. and Izenberg N.R., "Mercury's Complex Exosphere: Results from MESSENGER's Third Flyby", *Science*, **329**, 672 (2010)

[8] Boehnhardt H., Bibring J.P., Apathy I., Auster H.U., Finzi A.E., Goesmann F.,

Klingelhöfer G., Knapmeyer M., Kofman W., Krüger H. *et al.*, “The Philae lander mission and science overview”, *Phil. Trans. R. Soc. A*, **375**, 20160248 (2017)

[9] Ziegler J.F., Ziegler M. and Biersack J., “SRIM – The stopping and range of ions in matter (2010)”, *Nuclear Instruments and Methods in Physics Research Section B: Beam Interactions with Materials and Atoms*, **268**, 1818 (2010), 19th International Conference on Ion Beam Analysis

[10] Aumayr F. and Winter H., “Potential sputtering”, *Philosophical Transactions of the Royal Society of London A: Mathematical, Physical and Engineering Sciences*, **362**, 77 (2004)

[11] Wimmer-Schweingruber R.F., “The composition of the solar wind”, *Advances in Space Research*, **30**, 23 (2002)

[12] Szabo P.S., Chiba R., Biber H., Stadlmayr R., Berger B.M., Mayer D., Mutzke A., Doppler M., Sauer M., Appenroth J., Fleig J., Foelske-Schmitz A., Hutter H., Mezger K., Lammer H., Galli A., Wurz P. and Aumayr F., “Solar wind sputtering of wollastonite as a lunar analogue material – Comparisons between experiments and simulations”, *Icarus*, **314**, 98 (2018)

[13] Hijazi H., Bannister M., Meyer H., Rouleau C.M. and Meyer F., “Kinetic and potential sputtering of an anorthite-like glassy thin film”, *Journal of Geophysical Research: Planets*, **122**, 1597 (2017)

[14] Levinson A.A. and Taylor S.R., *Moon rocks and minerals: scientific results of the study of the Apollo 11 lunar samples with preliminary data on Apollo 12 samples*, Elsevier (2015)

[15] Szabo P.S., “Experimental and Simulated Sputtering of Gold, Iron and Wollastonite with a Catcher-QCM Setup”, *Diploma Thesis, TU Wien* (2017), unpublished

[16] Bame S., Asbridge J., Feldman W., Montgomery M. and Kearney P., “Solar wind heavy ion abundances”, *Solar Physics*, **43**, 463 (1975)

[17] Russell C., Luhmann J. and Strangeway R., *Space Physics: An Introduction*, Cambridge University Press (2016)

[18] Sigmund P., “Theory of sputtering. I. Sputtering yield of amorphous and polycrystalline targets”, *Physical review*, **184**, 383 (1969)

[19] Mutzke A., Schneider R., Eckstein W. and Dohmen R., “SDTrimSP Version 5.00”, *IPP report*, **12** (2011)

[20] Sauerbrey G., “Verwendung von Schwingquarzen zur Wägung dünner Schichten und zur Mikrowägung”, *Zeitschrift für Physik*, **155**, 206 (1959)

[21] Berger B., “Laboratory work on plasma-wall-interaction processes relevant for fusion experiments”, Ph.D. thesis, TU Wien (2017)

[22] *Physical Properties of Wollastonite* (2018.30.08), URL `http://imerys-additivesformetallurgy.com/wp-content/uploads/Physical-Properties-Overview.pdf`

[23] Bartzsch H., Glöß D., Frach P., Gittner M., Schultheiß E., Brode W. and Hartung J., “Electrical insulation properties of sputter-deposited SiO2, Si3N4 and Al2O3 films at room temperature and 400 °C”, *physica status solidi (a)*, **206**, 514 (2009)

[24] Galutschek E., “Development of a 14.5 GHz All-Permanent Magnet Multicharged ECR Ion Source for Remote Operation”, Ph.D. thesis, TU Wien (2005)

[25] Galutschek E., Trassl R., Salzborn E., Aumayr F. and Winter H., “Compact 14.5 GHz all-permanent magnet ECRIS for experiments with slow multicharged ions”, *Journal of Physics: Conference Series*, **58**, 395 (2007)

[26] Kowarik S., Hinderhofer A., Gerlach A. and Schreiber F., “5 - Modelling thin film deposition processes based on real-time observation”, in Z. Cao, ed., *Thin Film Growth*, Woodhead Publishing Series in Electronic and Optical Materials, 83 – 120, Woodhead Publishing (2011)

[27] Norton D.P., *Pulsed Laser Deposition of Complex Materials: Progress Toward Applications*, chapter 1, 1–31, Wiley-Blackwell (2006)

[28] Eckstein W., “Energy distributions of sputtered particles”, *Nuclear Instruments and Methods in Physics Research Section B: Beam Interactions with Materials and Atoms*, **18**, 344 (1986)

[29] Depla D., Mahieu S. and Greene J., “Chapter 5 - Sputter Deposition Processes”, in P.M. Martin, ed., *Handbook of Deposition Technologies for Films and Coatings (Third Edition)*, 253 – 296, William Andrew Publishing, Boston, third edition edition (2010)

[30] Berger B.M., Szabo P.S., Stadlmayr R. and Aumayr F., “Sputtering measurements using a quartz crystal microbalance as a catcher”, *Nuclear Instruments and Methods in Physics Research Section B: Beam Interactions with Materials and Atoms*, **406**, 533 (2017)

[31] Böngeler R., Golla U., Kässens M., Reimer L., Schindler B., Senkel R. and Spranck M., “Electron-specimen interactions in low-voltage scanning electron microscopy”, *Scanning*, **15**, 1 (1993)

[32] Hayderer G., Schmid M., Varga P., Winter H.P. and Aumayr F., “A highly sensitive quartz-crystal microbalance for sputtering investigations in slow ion–surface collisions”, *Review of Scientific Instruments*, **70**, 3696 (1999)

[33] Hayderer G., “Projectile charge state dependent sputtering of solid surfaces”, Ph.D. thesis, TU Wien (2000)

[34] Küstner M., Eckstein W., Dose V. and Roth J., “The influence of surface roughness on the angular dependence of the sputter yield”, *Nuclear Instruments and Methods in Physics Research Section B: Beam Interactions with Materials and Atoms*, **145**, 320 (1998)

[35] von Toussaint U., Mutzke A. and Manhard A., “Sputtering of rough surfaces: a 3D simulation study”, *Physica Scripta*, **2017**, 014056 (2017)

[36] Mortimer C.E. and Müller U., *Chemie: Das Basiswissen der Chemie; 126 Tabellen*, Georg Thieme Verlag (2007)

List of Figures

Danksagung

Ich möchte mich bei all jenen bedanken, die mich im Laufe meines Studiums auf ihre Weise unterstützt haben und mir mit Rat und Tat zur Seite gestanden sind.

Besonderer Dank gilt Prof. Dr. Friedrich Aumayr, der mich herzlich in seine Arbeitsgruppe aufgenommen hat und stets mit gutem Rat zur Seite stand. Die Selbstverständlichkeit, mit der er oft Ideen für Fragestellungen und Probleme parat hat, war und ist immer wieder beeindruckend. Auch die vorbildhafte Art und Weise, wie er seine Arbeitsgruppe leitet sucht ihresgleichen. Das Klima ist hervorragend und man kann sich sicher sein, immer auf Unterstützung zählen zu können.

Ein weiterer großer Dank geht an meinen Betreuer und Freund Paul Szabo, dessen Zielstrebigkeit und Ehrgeiz mir Vorbild sind, stetig an mir selbst zu arbeiten. Das gemeinsame Werken und Forschen hat mir sehr viel Freude bereitet, und selbst in schwierigeren Phasen gab es meist einen humorvollen Umgang und trotzdem etwas zu lachen.

Auch bei allen anderen Kolleginnen und Kollegen Anna Niggas, Daniel Mayer, Georg Harrer, Janine Schwestka, Reinhard Stadlmayr und Richard Wilhelm möchte ich mich für die vielen spannenden und unterhaltsamen Stunden bedanken.

Am meisten möchte ich mich bei meiner Familie bedanken. Meine Eltern Johanna und Gerhard haben mich stets darin bestärkt, das zu tun was mir Freude bereitet. Ohne ihre Unterstützung wäre ich nicht an diesem stolzen Punkt angekommen. Weiteres danke ich meiner Schwester Romana für den Rückhalt über die Dauer meines gesamten Studiums. Meine Freundin Anna ist seit unserer gemeinsamen Zeit immer für mich da und eine wichtige Stütze auf meinem Weg durchs Leben. Unser Sohn Ferdinand war mir in den letzten Monaten eine zusätzliche Motivation und bereichert mir mit seinem Lächeln jeden meiner Tage. Auch bei meiner Oma möchte ich mich vor allem für die andauernde finanzielle Unterstützung bedanken.

A. Appendix

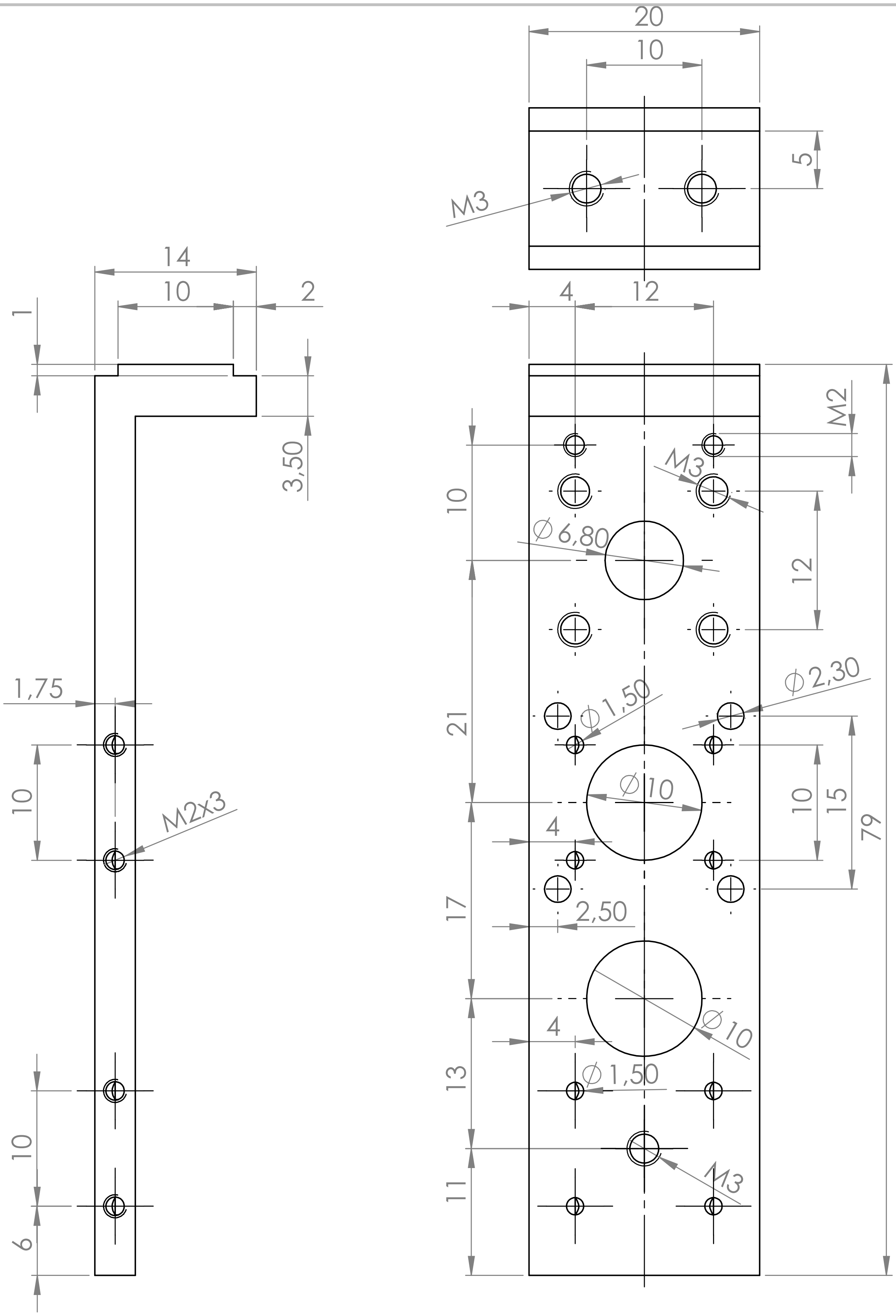

WENN NICHT ANDERS DEFINIERT:
BEMASSUNGEN SIND IN MILLIMETER
OBERFLÄCHENBESCHAFFENHEIT:
TOLERANZEN:
LINEAR:
WINKEL:

OBERFLÄCHENGÜTE:

ENTGRATEN UND SCHARFE KANTEN BRECHEN

ZEICHNUNG NICHT SKALIEREN

ÄNDERUNG

	NAME	SIGNATUR	DATUM
GEZEICHNET			
GEPRÜFT			
GENEHMIGT			
PRODUKTION			
QUALITÄT			

BENENNUNG:

Base_inkl_bulk

WERKSTOFF:

Edelstahl

GEWICHT:

ZEICHNUNGSNR.

A4

MASSSTAB:2:1

BLATT 1 VON 1

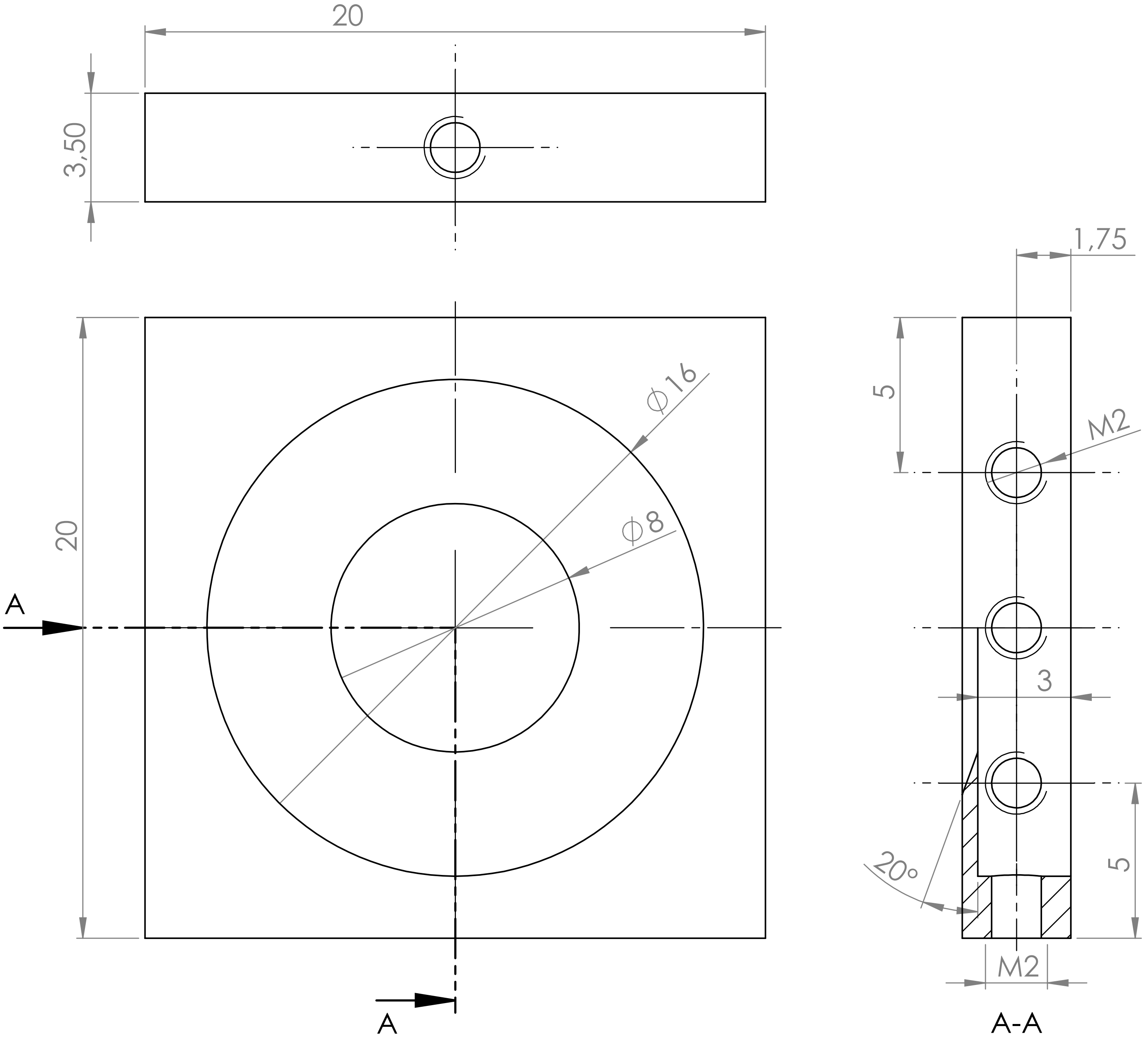

WENN NICHT ANDERS DEFINIERT:
BEMASSUNGEN SIND IN MILLIMETER
OBERFLÄCHENBESCHAFFENHEIT:
TOLERANZEN:
LINEAR:
WINKEL:

OBERFLÄCHENGÜTE:

ENTGRATEN
UND SCHARFE
KANTEN
BRECHEN

ZEICHNUNG NICHT SKALIEREN

ÄNDERUNG

	NAME	SIGNATUR	DATUM
GEZEICHNET	Berger		
GEPRÜFT	Kainz		
GENEHMIGT			
PRODUKTION			
QUALITÄT			

BENENNUNG:

WERKSTOFF:

GEWICHT:

ZEICHNUNGSNR. Frontplate_bulk

A4

MASSSTAB:5:1

BLATT 1 VON 1

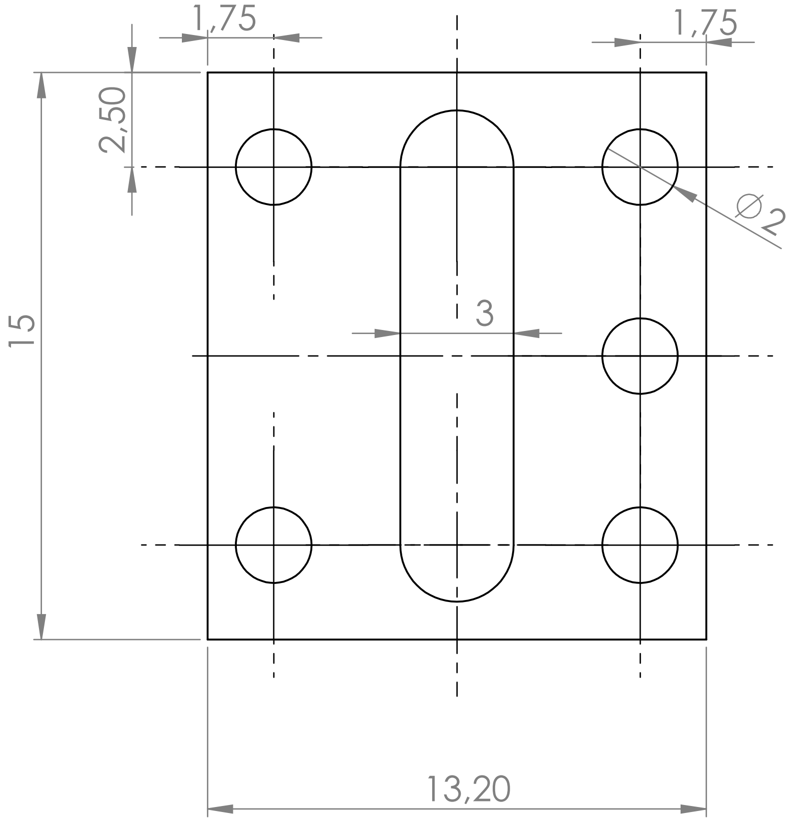

WENN NICHT ANDERS DEFINIERT:
BEMASSUNGEN SIND IN MILLIMETER
OBERFLÄCHENBESCHAFFENHEIT:
TOLERANZEN:
LINEAR:
WINKEL:

OBERFLÄCHENGÜTE:

ENTGRATEN
UND SCHARFE
KANTEN
BRECHEN

ZEICHNUNG NICHT SKALIEREN

ÄNDERUNG

	NAME	SIGNATUR	DATUM
GEZEICHNET			
GEPRÜFT			
GENEHMIGT			
PRODUKTION			
QUALITÄT			

BENENNUNG:

Distance_bulk

WERKSTOFF:

Edelstahl 1mm

GEWICHT:

ZEICHNUNGSNR.

A4

MASSSTAB:5:1

BLATT 1 VON 1